Thermometry and Thermal Transport in Micro/Nanoscale Solid-State Devices and Structures

David G. Cahill
Department of Materials Science and Engineering,
and the Frederick Seitz Materials Research Laboratory,
University of Illinois,
Urbana, IL 61801

Kenneth Goodson
Department of Mechanical Engineering,
Stanford University,
Stanford, CA 94305

Arunava Majumdar
Department of Mechanical Engineering,
University of California,
Berkeley, CA 94720
e-mail: majumdar@me.berkeley.edu

We review recent advances in experimental methods for high spatial-resolution and high time-resolution thermometry, and the application of these and related methods for measurements of thermal transport in low-dimensional structures. Scanning thermal microscopy (SThM) achieves lateral resolutions of 50 nm and a measurement bandwidth of 100 kHz; SThM has been used to characterize differences in energy dissipation in single-wall and multi-wall carbon nanotubes. Picosecond thermoreflectance enables ultrahigh time-resolution in thermal diffusion experiments and characterization of heat flow across interfaces between materials; the thermal conductance G of interfaces between dissimilar materials spans a relatively small range, $20<G<200$ MW m^{-2} K^{-1} near room temperature. Scanning thermoreflectance microscopy provides nanosecond time resolution and submicron lateral resolution needed for studies of heat transfer in microelectronic, optoelectronic and micromechanical systems. A fully-micromachined solid immersion lens has been demonstrated and achieves thermal-radiation imaging with lateral resolution at far below the diffraction limit, <2 μm. Microfabricated metal bridges using electrical resistance thermometry and joule heating give precise data for thermal conductivity of single crystal films, multilayer thin films, epitaxial superlattices, polycrystalline films, and interlayer dielectrics. The room temperature thermal conductivity of single crystal films of Si is strongly reduced for layer thickness below 100 nm. The through-thickness thermal conductivity of Si-Ge and GaAs-AlAs superlattices has recently been shown to be smaller than the conductivity of the corresponding alloy. The 3ω method has been recently extended to measurements of anisotropic conduction in polyimide and superlattices. Data for carbon nanotubes measured using micromachined and suspended heaters and thermometers indicate a conductivity near room temperature greater than diamond.
[DOI: 10.1115/1.1454111]

Keywords: Conduction, Heat Transfer, Interface, Measurement Techniques, Microscale, Nanoscale, Thin Films

1 Introduction

The last 50 years have witnessed the transformation of solid-state devices from objects of mere scientific curiosity to being at the heart of information technology. Electronic and optoelectronic devices are now so ubiquitous in modern society that their use often goes unnoticed. One of the main factors that has enabled this dramatic transformation is the ability to control the flow of charge in semiconductors. While charge flows only in metals and semiconductors, heat on the other hand flows in all materials. It is, therefore, natural to ask the question: What are the fundamental and engineering limits on the control of heat flow in solids?

Heat flow in solids occurs predominantly due to two energy carriers, namely, electrons in metals, and lattice vibrations or phonons in insulators and semiconductors. If one has to control their flow, one must recognize two fundamental length scales—wavelength and mean free path—associated with both electrons and phonons. One way to gain greater control of heat flow is to design and fabricate solid structures that overlap in size with the fundamental length scales. Table 1 lists the typical range of values for the length and time scales of electrons and phonons. It is obvious that size control of solid structures must occur at nanoscales. Modern manufacturing techniques allow us to fabricate structures that are confined to 2 (films), 1 (wires), or 0 (dots) dimensions with sizes in the 1–100 nm range. Hence, it is now possible, to some extent, to manipulate heat flow in solids through the interplay of confined size with electron/phonon wavelengths and mean free paths. Although much remains to be understood about heat flow in micro/nanostructures, significant progress has been made over the last decade or so. This could not have been possible without the development of new measurement techniques that allow one to probe heat flow at length and time scales comparable to those listed in Table 1. The purpose of this paper is twofold: (i) to provide a critical review of these measurement techniques and a discussion of future areas of development; and (ii) to present our current understanding of heat flow in micro/nanostructures and identify areas that need further research.

While greater control of heat flow might indeed be possible using confined structures, the following question is rather pertinent: Why is it important and what impact could it have? As the demands of information technology keep increasing, new engineering challenges continuously emerge. For example, the rapid increase in power density and speed of integrated circuits requires the use of unconventional materials. Figure 1(*a*) shows a micrograph of a polycrystalline diamond thin film grown by chemical vapor deposition on a silicon wafer [1]. The grain size and orientation, which depend on the details of the nucleation and growth processes, influence the thermal conductivities and thereby affect heat removal rate and response speed. Passivation materials in integrated circuits are often chosen for their ability to reduce elec-

Contributed by the Heat Transfer Division for publication in the JOURNAL OF HEAT TRANSFER. Manuscript received by the Heat Transfer Division July 27, 2001; revision received December 7, 2001. Associate Editor: V. K. Dhir.

Table 1 Typical length and time scales for energy carriers in solids at room temperature

	Electrons in Metal	Phonons in Insulators and Semiconductors
Wavelength, λ [nm]	0.1-1	1-5
Mean Free Path, ℓ [nm]	10	10-100
Relaxation Time, τ [s]	$(10\text{-}100)\times10^{-15}$	$(1\text{-}10)\times10^{-12}$
Propagation Speed, v [m/s]	$\approx10^{6}$	$(3\text{-}10)\times10^{3}$

tromagnetic cross-talk between neighboring interconnects and devices. However, they often have very low thermal conductivities. The importance of thermal properties of passivation materials in integrated circuits is illustrated by the metal-silicon contact in Fig. 1(*b*), whose temperature rise during rapid current transients is strongly influenced by heat diffusion into the bounding silicon dioxide [2]. One of the major breakthroughs in fiber optic communication is that of dense wavelength division multiplexing (DWDM) [3] in which a single optical fiber carries encoded information from about 100 lasers operating nominally at 1550 nm wavelength but with their wavelengths separated by about 0.4–0.8 nm. Figure 2 shows the cross-sectional view [4] of vertical-cavity surface-emitting laser (VCSEL) [5,6], which is made up of multiple layers of III–V semiconducting materials nanostructured

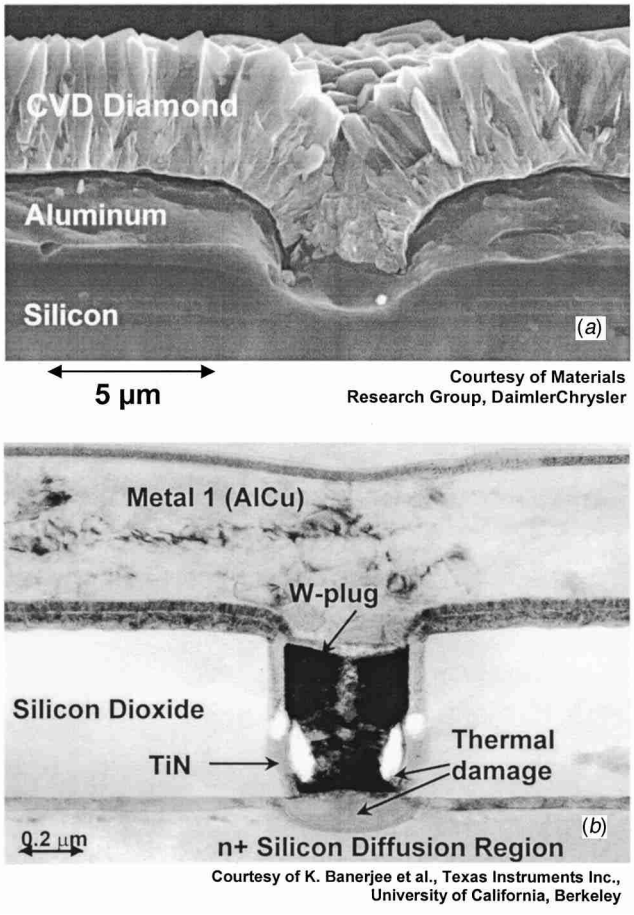

Fig. 1 Electron micrographs of novel electronic films and devices: (*a*) Diamond passivation film on aluminum. Diamond films are promising for enhanced heat removal from power integrated circuits and for fast thermal sensors. (*b*) Transmission electron micrograph of a VLSI metal-silicon contact, which has failed during a current pulse of sub-microsecond duration. The temperature rise is strongly influenced by the properties of the surrounding passive material.

in the 5–100 nm range. The maximum optical power output of these lasers depends critically on the heat removal rate. More importantly for DWDM, because the refractive index of the III–V materials is temperature dependent, the output wavelength varies with temperature at about 0.1 nm/K, which can lead to cross-talk between channels. Hence, it is necessary to actively control their temperature, which requires one to develop solid-state cooling devices. Figure 3 shows an array of thermionic microcoolers fabricated on a silicon wafer [7]. The cross-section of this device shows that it contains a Si/SiGe superlattice with a period of about 10 nm. The purpose of this superlattice is to minimize heat flow between the cold and hot ends of the refrigerator. This leads to the question as to why such solid-state refrigerators and engines cannot replace their macroscopic vapor based ones.

It is often forgotten that when semiconductors were first discovered, the initial excitement about their use was not for electronics but for refrigeration [8]. The reason we do not generally use solid-state energy conversion is because of their low device performance. This depends on the non-dimensional thermoelectric figure of merit of a material, $ZT=S^2\sigma T/k$, where S is the Seebeck coefficient, σ is the electrical conductivity, and k is the thermal conductivity. Currently, compounds such as Bi_2Te_3 offer the best ZT ($ZT\approx1$) at room temperature, which leads to coefficient of performance of refrigerators of about unity. If ZT could be increased to 3, the performance of thermoelectric refrigerators or power generators could be comparable to their gas-based counterparts. Although it is possible to control S and σ by doping a semiconductor, significant reduction of k has not been possible in the past. Recent studies have shown that by nanostructuring a solid, it would be possible to simultaneously increase $S^2\sigma$ and reduce k and thereby increase its ZT value to 3 or more [9]. This, by itself, is a compelling reason to study heat flow in micro/nanostructured solids.

The paper is divided into two main sections, one on thermometry at short length and time scales and the other on thermal transport in low-dimensional structures.

2 Thermometry

During the last decade, remarkable progress has been made in the area of microscale thermometry, which can now allow temperature measurements at length and time scales comparable to the mean free paths and relaxation times of energy carriers in solids (see Table 1). This section provides a critical review of three thermometry techniques, namely: (i) scanning thermal microscopy for high spatial resolution thermal imaging; (ii) picosecond reflectance thermometry for measuring thermal properties of interfaces and nanostructures; and (iii) scanning optical thermometry that combines high spatial and temporal resolution measurements.

2.1 Scanning Thermal Microscopy. A scanning thermal microscope (SThM) operates by bringing a sharp temperature-sensing tip in close proximity to a sample solid surface (see Fig. 4). Localized heat transfer between the tip and sample surface changes the tip temperature. By scanning the tip across the sample surface, a spatial distribution of the tip-sample heat transfer is mapped out. When the tip comes in local equilibrium with the sample, one obtains the spatial temperature distribution of sample surface, whereas if the temperature change in determined for a known heat flux, one could obtain the local thermal properties. The spatial resolution depends mainly on three factors, namely, tip sharpness, tip-sample heat transfer mechanism, and the thermal design of the probe. In the recent past, the spatial resolution has been improved to 30–50 nm, allowing one to study thermal transport phenomena at these length scales.

The idea of SThM was first proposed by Williams and Wickramasinghe [10] when they used a thermocouple at the end of a metallic wire to measure temperature. Tip-sample heat transfer was used to image the surface topography of electrically insulating materials. Since then, significant progress has

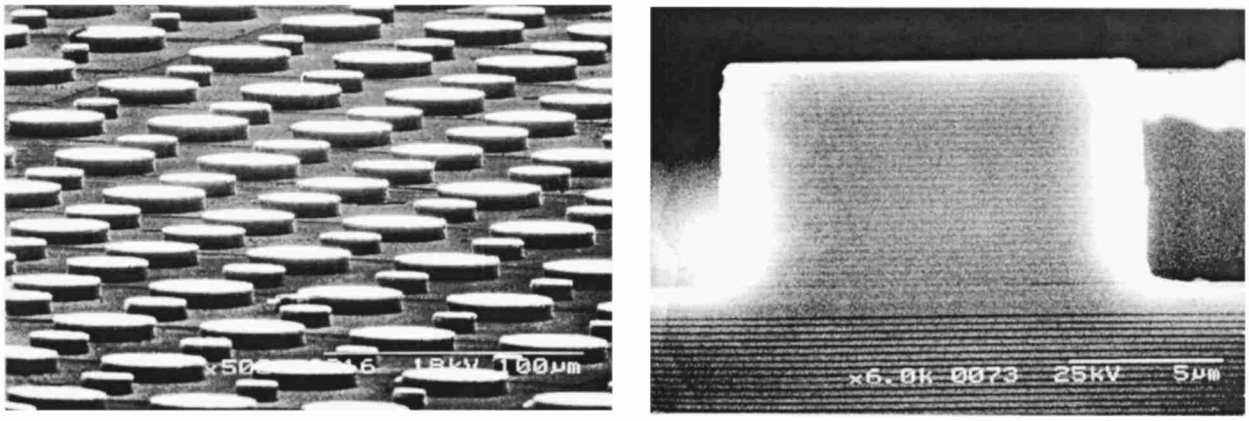

Fig. 2 Electron micrographs of (left) an array of vertical cavity surface emitting lasers (VCSEL) on a single wafer and (right) the cross of an individual VCSEL. Each laser contains multiple layers of III–V semiconductor materials which are approximately 60–100 nm in the Bragg mirrors of the laser or 1–10 nm in the active quantum well region.

been made in improving thermocouple-based measurements [11,12,13,14,15,16,17,18,19], while other techniques based on contact potential [20], electrical resistance [21,22,23,24] and thermal expansion [25,26,27] have also been developed. Although the first study utilized a wire probe [10,11], most of the subsequent development has been towards cantilever-based probes such that atomic force microscopes (AFMs) [28] could be used as a platform for SThM. Figure 4 shows a schematic diagram of an AFM, which utilizes a sharp tip mounted on a cantilever to be scanned across a sample surface. Cantilever deflections are measured by reflecting a laser beam off the cantilever and onto a position-sensitive photodiode. The deflection signal is used in a control system to maintain a constant tip-sample contact force while the tip is scanned laterally. When a temperature sensor is mounted on the very apex of the tip, such probes can be used to image both the topography and the temperature distribution of devices such as single transistors [12,13,29] and vertical cavity lasers [30]. Such studies have helped in identifying defects and failure mechanisms while providing insight about electron, photon and phonon transport in these devices. In addition, SThM has also been used to measure thermal properties of materials and perform calorimetry at nanometer scales [14,16,20,22,23,24,31]. Progress in this field till 1999 has been documented in a comprehensive review [32]. Since then, however, there have been some significant breakthroughs in both probe design and fabrication, and heat transfer studies at nanoscales [33].

The thermal design of the cantilever probes is extremely important for SThM performance. The thermal resistance network in Fig. 4 suggests that for a given ambient temperature, T_a, and sample temperature T_s, the tip temperature T_t, can be written as $T_t = T_s + (T_a - T_s)/(1+\phi)$, where $\phi = (R_c + R_t)/R_{ts}$ is the ratio of the cantilever thermal resistance, R_c, plus the tip resistance, R_t, with respect to the tip-sample thermal resistance, R_{ts}. The cantilever and tip resistance arises from both conduction through the tip and cantilever material as well as the surrounding air, while the tip-sample resistance results from liquid, air and solid-solid conduction. Changes in sample temperature can be related to changes in the tip temperature as $\Delta T_t/\Delta T_s = \phi/(1+\phi)$. This relation suggests that the accuracy and sensitivity of sample temperature measurement by the tip depend on ϕ, which must be large for better SThM performance. The spatial resolution, Δx, of SThM measurements can be expressed as $\Delta x = \Delta T_n/(dT_t/dx)$ where ΔT_n is the noise in the temperature measurement and dT_t/dx is the mea-

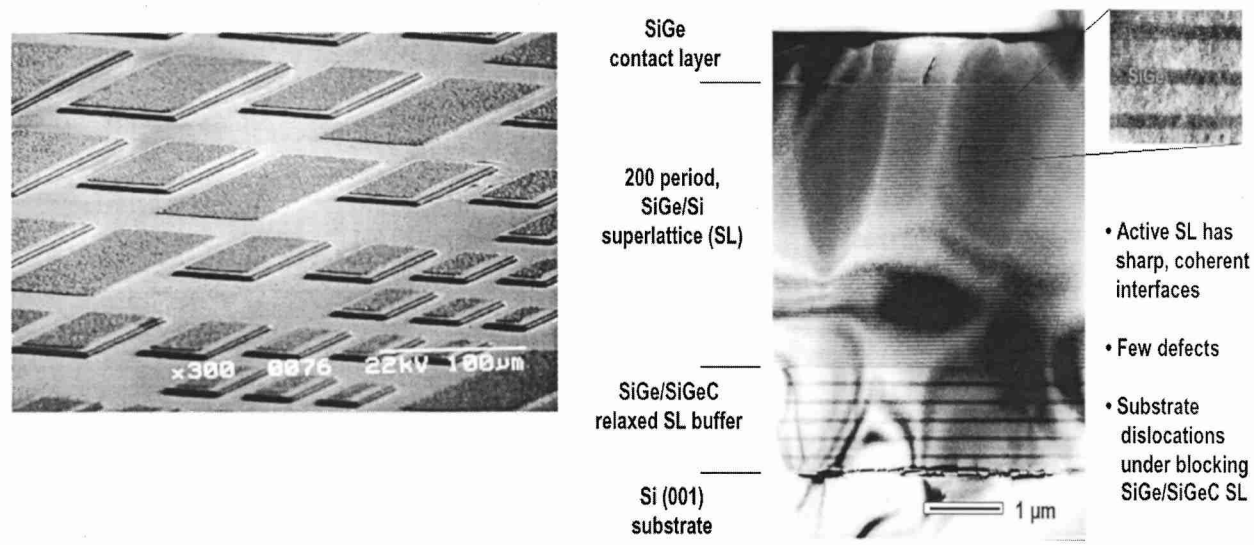

Fig. 3 Electron micrographs of (left) an array of SiGe superlattice thermionic microcoolers on a single wafer and (right) the cross section of a single device showing the SiGe/Si superlattice structure. The superlattice period is approximately 10 nm.

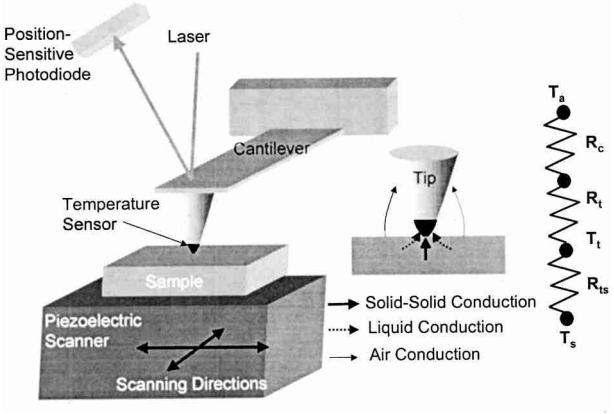

Fig. 4 Schematic diagram of a scanning thermal microscope (SThM). It consists of a sharp temperature sensing tip mounted on a cantilever probe. The sample is scanned in the lateral directions while the canitilever deflections are monitored using a laser beam-deflection technique. Topographical and thermal images can be thermally obtained. The thermal transport at the tip-sample contacts consists of air, liquid and solid-solid conduction pathways. A simple thermal resistance network model of the sample and probe combination shows that when the sample is at temperature T_s, the tip temperature T_t depends on the values of the thermal resistances of the tip-sample contact, R_{ts}, the tip, R_t, and the cantilever probe, R_c.

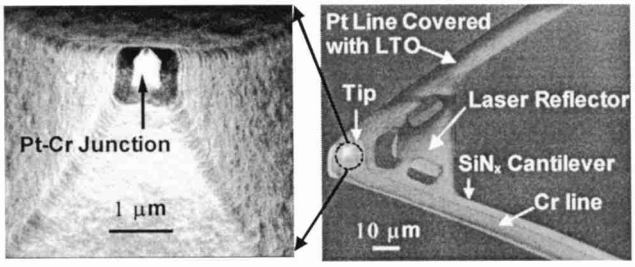

Fig. 5 Electron micrographs of a two-armed cantilever probe with a pyramid-shaped tip at the free end. The tip contains a Pt-Cr thermocouple junction at its apex which is approximately 500 nm in lateral size.

sured temperature gradient. Because the tip and sample temperatures are related through ϕ, the spatial resolution can be expressed as

$$\Delta x = \frac{\Delta T_n}{(dT_s/dx)}\left(\frac{1+\phi}{\phi}\right). \tag{1}$$

Equation (1) clearly suggests that small values of ϕ lead to poor spatial resolution of SThM. While the contributions of both air and solid conduction to R_c and R_t depends on probe geometry, that for solid conduction depends critically on the thermal conductivity of tip and cantilever material. Shi et al. [34] have performed elaborate modeling of air and solid conduction between the sample and the cantilever probe, including microscale effects near the tip-sample contact, to study the effects of material properties and probe geometry on R_c and R_t. This has provided a framework for designing SThM probes.

One of the most challenging problems in SThM is probe fabrication. Initial studies had focused on etched wire probes [10,11,12,13,14], although the high thermal conductivity of metal wires as well as irreproducibility and the large sensor size led to inaccuracies and lack of resolution. This led to development of thin film probes that could be microfabricated. However, to achieve the nanoscale sensor size at the apex of the tip, nontraditional lithography techniques had to be used, which required the probes to be made one at a time [15,17]. Subsequently, batch fabricated probes were developed, first based on e-beam lithography [19] and later using standard photolithography-based MEMS fabrication techniques [34]. Details of the design process and fabrication process can be found in Shi et al. [34]. Figure 5 shows electron micrographs of a probe [34] containing two cantilever arms a Pt-Cr thermocouple junction at the apex of the pyramid-shaped tip. The tip radius is generally about 50–100 nm while the thermocouple size can be controlled between 100–500 nm in height.

A fundamental understanding of tip-sample heat transfer mechanisms is crucial for quantitatively probing nanostructures using SThM. Although researchers initially thought heat transfer to be dominated by solid-solid and air conduction, the phenomenon turned out to be more complex. One of the surprising discoveries was that of the role of liquid film conduction. A solid surface is generally covered with a very thin layer (a few monolayers thick) of a liquid film under ambient conditions: water for hydrophilic surfaces and some hydrocarbon for hydrophobic ones. When the tip comes in contact with the sample, the liquid film forms a meniscus and bridges the tip and the sample. It was first proposed by Luo et al. [17] that this liquid film dominated tip-sample heat transfer for nanoscale point contacts, and suggested a heat transfer coefficient $h \approx 10^9$ W/m^2-K. The actual conductance depends on the radius of curvature of the tip apex. More recently, Shi et al. [35] have shown using the probes in Fig. 5, that while liquid film does play an important role, solid-solid and air conduction pathways are equally important. Figure 6 plots the cantilever deflection and the tip temperature as a function of tip-sample relative position. The measurements show that before the tip is brought into contact, air conduction dominates heat transfer. As the tip makes contact with the sample surface, liquid film conduction results in a sudden jump in tip temperature due to a marked increase in thermal conductance. Subsequently, the tip temperature rises gradually as the contact force is increased indicating the role of solid-solid conduction. Beyond a certain force, the tip temperature saturates to a constant value, which arises from the fact that the tip-sample contact area becomes constant. From this data, values of liquid, solid-solid and air conductances can be determined [35]. Although this is a typical thermal behavior of SThM probes, the exact values of forces and thermal conductances at different transition points depends on the probe design. The thermal time constant of probes shown in Fig. 5 during contact with a sample was shown to be on the order of 10 μs [34], which can allow a measurement bandwidth of about 100 kHz [36].

Figure 7 shows topographical and thermal images of the cross-section of a vertical cavity surface emitting laser (VCSEL) [30]. Because the refractive index of the III–V semiconducting materials used in VCSELs is temperature dependent, the output wavelength of VCSELs varies with temperature at about 0.1 nm/K. Hence, not only is it necessary to actively control the temperature of these devices [7], fundamental understanding of thermal phenomena inside the devices is also important. SThM images of a VCSEL showed that the maximum temperature occurred at the quantum well region where electrons and holes recombine radiatively. This suggested non-radiative recombination due to the presence of defects and crystal imperfections to be the dominant loss mechanism as opposed to other mechanisms such as Joule heating and radiative absorption. The temperature distribution also suggested a thermal lens formation due to the temperature dependence of the refractive index of these materials.

Carbon nanotubes have recently been intensively studied for their electrical, thermal, mechanical, and chemical properties [37]. They come in two kinds: multiwall carbon nanotubes (MWCNs), which are generally about 10 nm in diameter, and single wall carbon nanotubes (SWCNs) which are about 1–2 nm in diameter.

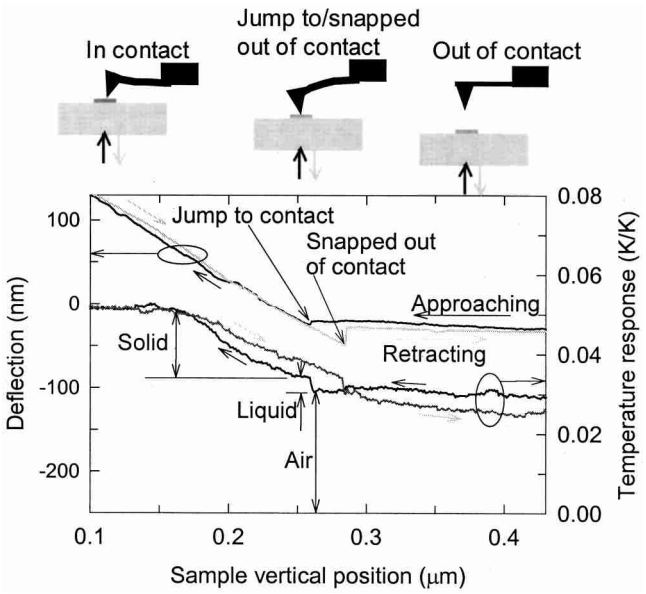

Fig. 6 Cantilever deflection and temperature response of the probe as a function of sample vertical position. The sample was a 350 nm wide electrically heated metal line. When the sample approaches the tip, the cantilever deflection remains unchanged till a jump to contact. During this time, the tip temperature rises very gradually due to air conduction. Corresponding to jump to contact the tip temperature suddenly rises due to liquid conduction. As the sample is pushed up the cantilever deflects linearly, while the tip temperature increases linearly due to increase in solid-solid contact area to a certain constant value. When the sample is retracted away, the solid-solid conductance decreases, but at a different rate, indicating some hysteresis due to plastic deformation of the tip or the sample. The tip remains in contact for a longer duration due to surface tension forces. When the tip snaps out of contact from the sample, there is a sudden drop in temperature due to loss of liquid film conduction.

MWCNs are generally metallic in nature, while SWCNs can be both metallic and semiconducting depending on the chirality in their crystal structure. Although there have been several studies on electrical transport in MWCNs and SWCNs there are several unanswered questions regarding dissipation in these nanostructures. While current flow in MWCNs is expected to be diffusive leading to uniform Joule heating, there is speculation that electron transport in SWCNs is ballistic over several micrometers in length even at room temperatures. Figure 8(*a*) shows topographical and thermal images of an electrically heated MWCN of 10 nm diameter [33,38]. The spatial resolution of SThM was about 50 nm. Detailed modeling of the measured temperature combined with an understanding of tip-sample heat transfer mechanism was used to quantitatively determine the actual temperature rise of the MWCN [33]. The temperature profile along the length of the MWCN was parabolic, indicating a uniform Joule heating and diffusive electron transport. Figure 8(*b*) shows the topographical and thermal images of a SWCN that was about 1 nm in diameter. Thermal images at low voltages showed that most of the temperature rise was near the contacts, indicating ballistic electron flow in the SWCN. At high voltages, however, bulk dissipation started to occur as indicated by the thermal images. This is presumably because of optical phonon emission by electrons when they get highly energized by transport in high electric fields [39].

There have been several important developments and breakthroughs in SThM over the last decade, which are now allowing us to routinely make thermal measurements at spatial resolutions in the sub-100 nm regime. There are three main areas where progress could be made in the future, namely: (i) fundamental understanding of tip-sample heat transfer and accuracy of temperature measurements; (ii) design and fabrication of integrated multifunctional probes; (iii) thermal probing of new devices and micro/nanostructures. Although we have made progress in our understanding of heat transfer at point contacts [17,35,40], there are still many fundamental issues unresolved. For example, can the effect of liquid conduction be controlled by tailoring surface chemistry? What is the role of near-field radiation in tip-sample heat transfer [41,42,43], especially in vacuum environment? How do phonons and electrons propagate through a point contact that is on the order of their wavelength? Can we conduct SThM experiments at low temperature and observe quantum transport effects? Because tip-sample thermal resistance depends on surface topography, topography-related artifacts in thermal images still remains a problem. There are two potential solutions: a thorough knowledge of tip-sample heat transfer in order to model the effect of topography; or a null-point measurement such that tip-sample temperature difference can be mini mized thereby eliminating any heat flow. The latter requires more sophisticated probes with multiple sensors and feedback control.

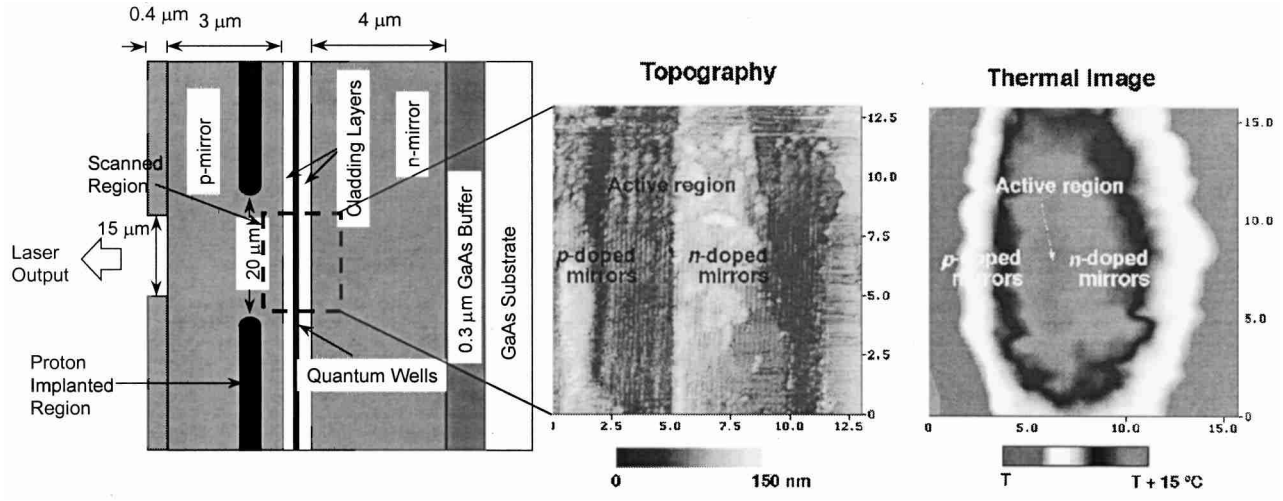

Fig. 7 (left) Schematic diagram, (middle) topographical image, and (right) thermal image of the cross-section of a vertical cavity laser. The region imaged is approximately 6 μm on either side of the active quantum well region, which includes the p-doped and n-doped Bragg mirrors consisting of alternating layers of AlAs and AlGaAs. The thermal image was obtained after a current was applied and the device was lasing.

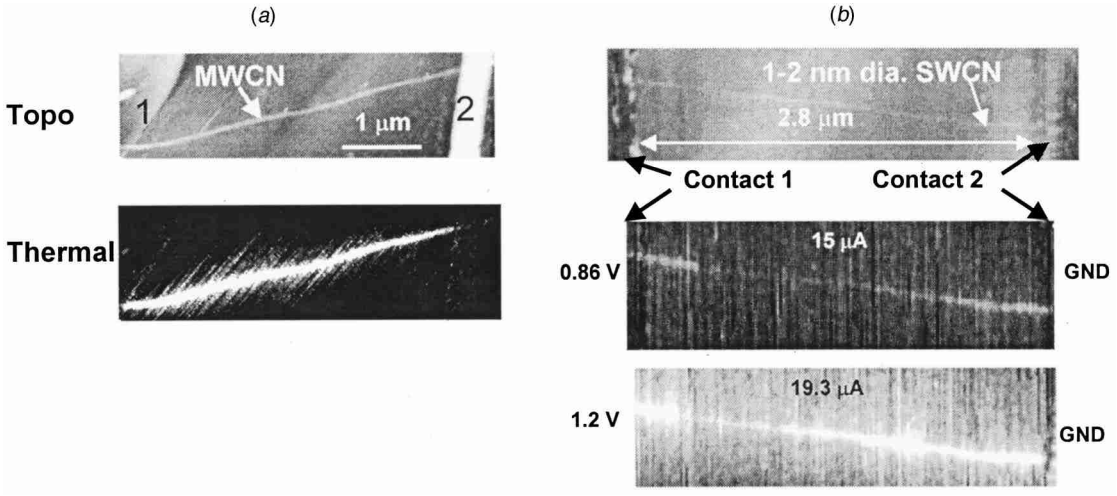

Fig. 8 Topographical and thermal images of electrically heated: (*a*) multiwall carbon nanotube (MWCN) about 10 nm in diameter with 22.4 μA flowing through it; (*b*) single wall carbon nanotube (SWCN) 1-2 nm in diameter with 15 μA (top) and 19.3 μA flowing through it. The temperature profile of the MWCN is parabolic in nature indicating a diffusive flow of electrons. At low bias, the SWCN is heated only at the contacts suggesting ballistic flow, while at higher bias the SWCN is heated in the bulk, most likely due to optical phonon emission. All measurements were made at room temperature.

The development of batch fabrication processes for making SThM probes [19,34,44,45] has made them readily available to many researchers, which itself is a significant engineering contribution. Currently, however, one can place only a single temperature sensor on SThM tips. Future progress will be driven towards multiple sensors and actuators on integrated cantilever probes such that one could simultaneously measure temperature and heat flux as well as electrical, optical and other nanoscale properties while imaging a nanostructure. Finally, because new nanoscale materials and energy conversion devices are being developed, there will also remain a need to thermal probe them at nanoscales. For example, thermoelectric properties of nanostructured semiconductors are markedly different from their bulk properties [46]. By simultaneously measuring thermal, electrical, and thermoelectric properties using a multifunctional SThM, one could characterize low-dimensional nanostructures. An area of research that is largely unexplored is SThM under liquid environment, in particular, of biological molecules. Proteins and DNA undergo structural changes and phase transitions at different temperatures. Localized calorimetry of molecules could shed light on the binding behavior of biomolecules.

2.2 Picosecond Reflectance Thermometry. Reflectance thermometry can be extended to picosecond time-scales using mode-locked lasers; mode-locked laser typically produce a series of <1 ps pules at a repetition rate of $\approx$76 MHz. Extremely high time resolution is achieved by splitting the laser output into two beam paths, a ''pump'' beam and a ''probe'' beam, and adjusting the relative optical path lengths with a mechanical delay stage. If the sample under investigation is metallic, or can be coated with a thin metal film, then a small fraction of the energy from each pulse in the pump beam produces a sudden jump in temperature near the surface of the sample. The decay of the near-surface temperature is then interrogated by the reflected energy of the series of pulses in the probe beam. Typically, the intensity of the pump beam is modulated and variations in the intensity of the reflected probe beam at the modulation frequency are measured with an rf lock-in-amplifier.

In 1986, Paddock and Eesley [47] described the first thermal transport experiments using picosecond thermoreflectance; their primary motivation—providing a direct method for measuring heat diffusion on nanometer length scales—remains valid today. Most engineering materials have thermal diffusivities D in the range $0.005<D<1$ cm^2 s^{-1} and at $t=200$ ps, heat diffusion lengths $\ell=\sqrt{(Dt)}$ are in the range $10<1<140$ nm. Therefore, picosecond time resolution offers nanometer-scale depth resolution and, more specifically, picosecond thermoreflectance can isolate the effects of interface conductance from the thermal conductivity of a thin layer. By contrast, thermoreflectance using Q-switched lasers [48] and the 3ω method [49] cannot distinguish between the thermal conductivity of a film and the thermal conductance of its interfaces. Greater understanding of energy transport on picosecond time-scales could also enhance capabilities for thin-film metrology. Picosecond acoustics using pump-probe optical techniques is a powerful tool for determining film thickness; in some cases, picosecond thermoreflectance could provide complementary data on film and interface microstructure [50].

Despite the promise of these methods, only a few quantitative and systematic studies of thermal properties of materials have used picosecond optical techniques [47,51,52,53,54,55]. Experiments by Maris and co-workers on interface thermal conductance [52] and superlattice conductivity [54] are the most complete. Data for the thermal decay at short times $t<50$ ps are difficult to interpret quantitatively because (i) hot-electrons can deposit energy outside of the optical absorption depth, (ii) the temperature dependence of the complex index of refraction $d\tilde{n}/dT$ is typically unknown, (iii) the diffusion equation fails on length scales comparable to the mean-free-paths of the dominant energy carriers, and (iv) the assumption of equilibrium between phonons and electrons is not always valid. At long times $t>500$ ps, measurements are often plagued by shifts in the focal plane and beam overlap created by large displacements of the delay stage. (Capinski and Maris describe a method for improving accuracy at long delay times [56].) We are optimistic, however, that improved performance and dropping costs of solid-state mode-locked lasers will expand applications of picosecond thermoreflectance. Reliable, low-noise Ti:sapphire lasers that produce 100 fs pulses are commercially available and can be operated with only a modest knowledge of the technology of ultra-fast lasers.

An example apparatus in use at the Laser Facility of the Frederick Seitz Materials Research Laboratory is shown in Fig. 9. The optical design contains some unique features: a single microscope objective focuses the pump and probe beams, collimates the reflected probe beam, and forms a dark-field microscopy image of the sample surface on a CCD camera. The integrated dark-field optical microscope greatly facilitates focusing and alignment of

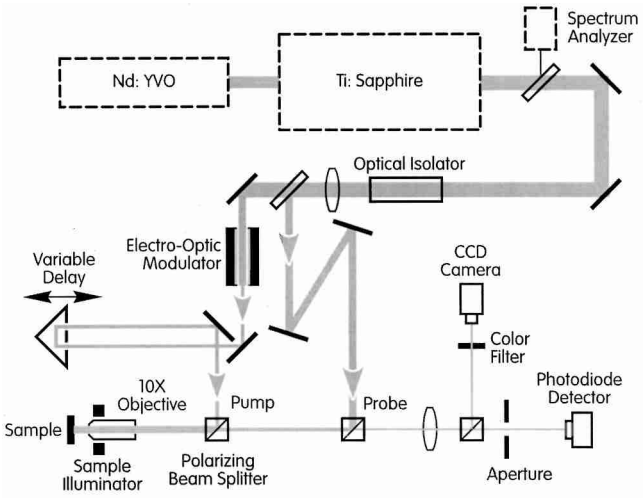

Fig. 9 Picosecond thermoreflectance and acoustics apparatus at the University of Illinois using a single objective and an integrated dark-field microscope. The pump and probe beams are parallel at the back-focal-plane of the objective lens but offset by ≈ 4 mm. The aperture in front of the detector rejects the small fraction of pump beam that leaks through the polarizing beam splitter.

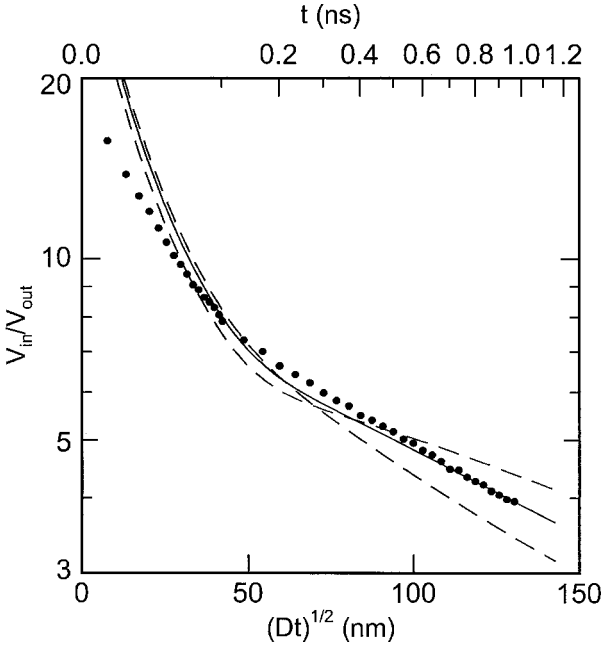

Fig. 10 Picosecond thermoreflectance data (solid circles) for thermal transport through an epitaxial TiN/MgO(001) structure at room temperature. The ratio of the in-phase to out-of-phase signals of the lock-in amplifier at $f=9.8$ MHz is plotted as function of the thermal diffusion length in TiN; the delay time t is given on the top axis. The TiN layer thickness is 100 nm. We assume that the thermal conductivity of the TiN film is given by the Wiedemann-Franz law, $\Lambda = LT/\rho = 58$ W m^{-1} K^{-1}; the thermal conductivity of MgO is 51 W m^{-1} K^{-1}. The solid and dashed lines are fits to the data using Eq. 3 with one free parameter, the interface thermal conductance G. The solid line is the best fit, $G=0.42$ GW m^{-2} K^{-1}. The upper and lower dashed lines are for $G=0.2$ and $G=1.0$ GW m^{-2} K^{-1}, respectively.

the pump and probe beams. The $1/e^2$ beam diameter at the sample is relatively large, 15 μm for both pump and probe.

In a modulated pump-probe experiment, the differences in reflected probe intensity caused by the pump pulse appear at the modulation frequency of the pump beam and are extracted with lock-in detection. But interpretation of this lock-in signal is not completely straightforward, particularly as the time delay becomes a significant fraction of the separation between pulses. Following Ref. [56], the lock-in response V_{LI} of a modulated pump-probe reflectivity measurement is

$$V_{LI}(t) = \frac{\alpha}{\tau} \sum_{q=-\infty}^{\infty} \exp(i2\pi f(q\tau + t)) \Delta R_1(q\tau + t), \qquad (2)$$

where the real part of V_{LI} is the in-phase signal of the lock-in amplifier V_{in} and the imaginary part of V_{LI} is the out-of-phase signal V_{out}; α is a constant, τ the time between pulses (typically ≈ 13 ns), f the modulation frequency, t the time delay of the probe beam, and $\Delta R_1(t)$ is the reflectivity change at a time t following an excitation of the sample by a single pump pulse. In Ref. [56], the authors state that Eq. 2 is valid only in the limit $f\tau \ll 1$ but we have found that Eq. 1 is an exact solution for all values of $f\tau$ as long as the lock-in time constant τ_{LI} satisfies $f\tau_{LI} \gg 1$. Typically, comparisons of experimental data and the prediction of Eq. 2 are used to optimize free parameters in a thermal model; for all but the shortest times, the temperature is homogeneous through the optical absorption depth of the thin metal film and $\Delta R_1(t) = (dR/dT)\Delta T_1(t)$. The surface temperature $\Delta T_1(t)$ can be accurately calculated using one-dimensional heat flow since the thermal diffusion length is usually much smaller than the radius of the focused pump beam [56].

Although Bonello and co-workers [57] discuss the in-phase signal at $t<0$, to the best of knowledge, no prior work has made use $V_{\text{out}}(t)$. But the extra information in the out-of-phase signal may provide a simple method of correcting for non-idealities in the experiment: both the in-phase and out-of-phase signals will be changed by the same amount by defocusing of the pump beam and changes in the pump-probe overlap and so the ratio of $V_{\text{in}}/V_{\text{out}}$ is often a more robust quantity than V_{in} alone. $V_{\text{out}}(t)$ varies weakly with t but decreases with modulation frequency f; we choose $f \approx 10$ MHz to minimize radial heat flow without sacrificing too much signal in V_{out}.

A frequency domain version of Eq. 2 is sometimes more convenient: instead of starting with the time domain response to a pump pulse $\Delta T_1(t)$, we calculate the frequency domain response $\Delta T(\nu)$ of a multilayer sample using matrix methods [58]. With the probe beam delayed by a time t, the ratio of the two lock-in signals is then

$$\frac{V_{in}(t)}{iV_{out}(t)} = \frac{\sum_{q=-\infty}^{\infty} (\Delta T(q/\tau + f) + \Delta T(q/\tau - f)) \exp(i2\pi tq/\tau)}{\sum_{q=-\infty}^{\infty} (\Delta T(q/\tau + f) - \Delta T(q/\tau - f)) \exp(i2\pi tq/\tau)}. \qquad (3)$$

If the pump beam is advanced instead of delaying the probe, (see Fig. 9), Eq. 3 must be corrected by a phase factor that is equivalent to shifting the phase of the lock-in reference channel by $2\pi ft$.

Figure 10 shows an example of this approach using data for an epitaxial TiN layer deposited on MgO by reactive magnetron sputtering at 800°C. Because TiN and MgO have the same crystal structure (fcc NaCl) and almost identical lattice constants, we expect that these TiN/MgO interfaces are more perfect than typical metal/ceramic interfaces. TiN is a ''metallic ceramic'', a hard, refractory material with metallic electrical properties. Our thermal model assumes that the heating produced of the pump pulse can be approximated by an instantaneous deposition of energy uniformly distributed through the optical absorption depth of TiN, $\lambda/(4\pi k) = 16$ nm. Since we assume $\Delta R(t) = (dR/dT)\Delta T(t)$, the

fit at short times is poor; i.e., we have not accounted for gradients in $\tilde{n}$ within the optical absorption depth [59]. At long times, we obtain an excellent one-parameter fit to the data but the data are relatively insensitive to the property we are interested in, the thermal conductance of the interface G: changing G by a factor of 2 produces only a $\approx$15 percent change in V_{in}/V_{out} at $t=1$ ns.

2.3 Scanning Optical Thermometry. The optical thermometry described in section 2.2 uses brief laser pulses to excite and interrogate a surface. The radiation is generally not strongly focused, which allows one-dimensional transport modeling normal to the absorbing surface. For micro and nanoscale semiconductor devices, sensors, and actuators, the goal is to measure temperature distributions resulting from *electrical* heating with simultaneously high spatial and temporal resolution. In contrast to the scanning probe methods described in section 2.1, most optical thermometry methods directly probe the microdevice without requiring heat diffusion into a solid sensor. This eliminates the associated delay and, in principle, allows measurements in the picosecond regime as discussed in section 2.2. Pump-probe microdevice thermometry with picosecond temporal resolution could be achieved using a photodiode to convert the pump pulse into an electrical current. This electro-optic excitation approach is well established for measuring electric field distributions and the voltage step response in semiconductor devices [60,61]. However, the fastest optical thermometry of electrically-heated devices used steady-state radiation and yielded temporal resolution, limited by noise and calibration complications, near 1 ns.

There has been extensive research on microdevice optical thermometry. Most measurements use visible or near-visible radiation with far-field optics, which provide diffraction-limited spatial resolution near 1 μm [62]. Examples include micro-Raman thermal imaging, for which the ratio of the Stokes and anti-Stokes lines determined the steady-state optical phonon temperature in the semiconducting regions of quantum well lasers [63] and silicon field-effect transistors [64]. Picosecond Raman thermometry of solvent-solute mixtures at large spatial dimensions [65] could be extended to microdevices. Expansion thermometry [66,67,68] used radiation interference or dilation to probe thermal expansion and temperature fields in the near-surface region. The extraction of temperature fields from surface displacement is very difficult in the absence of a dedicated surface layer with high thermal expansion coefficient, as discussed for Joule expansion microscopy using the AFM in section 2.1. The temperature dependence of photon-induced emission provides another opportunity for thermometry, although the governing electron-photon relaxation processes can limit temporal resolution. Example studies used temperature-induced shifts in the photoluminescence spectra of semiconductors [69] or, for the case of a dedicated thin-film coating, a shift in the fluorescence efficiency [70].

Thermoreflectance imaging detects temperature changes through the optical reflectance [71] and has been applied to micromachined structures [72,73,74,75]. Precise scanning of the laser focus spot over the microdevice during periodic electrical heating yields the full-field transient temperature [76]. Figure 11(*a*,*b*) show the experimental setup and temperature distribution data across the corner of an aluminum-copper alloy interconnect [77]. The temperature distribution was captured 100 ns after the initiation of an electrical current pulse and is consistent with a coupled analysis of the temperature and potential distributions in the metal. The diffraction-limited spatial resolution is comparable with the radiation wavelength of 800 nm, which was chosen to optimize the thermoreflectance coefficient, C_{TR}. Although metals have relatively low thermoreflectance coefficients, $C_{TR} \sim 10^{-5}$ K^{-1}, they are well suited for thermoreflectance imaging because their small penetration depths isolate the volume over which radiation-surface interactions are occurring and minimizes the impact on the electrical behavior of the device. The thermoreflectance coefficients of aluminum and copper achieve maxima near 800 nm and 577 nm, respectively, owing to associated high probabilities for electron interband transitions [78,79]. Because the thermoreflectance coefficient can depend on the radiation spot size, a two-step calibration procedure on a dedicated, similar micromachined structure subjected to transient electrical heating and thermometry is helpful for obtaining the relevant value of C_{TR} [76]. Reflectance thermometry can be performed through transparent passive layers, such as silicon dioxide. However, temperature and refractive index gradients in the overlayer effectively limit the temporal resolution to the thermal diffusion time normal to that layer.

Optical thermometry below the diffraction limit remains immature. From the far field, radiation with vacuum wavelength λ can be focused to a spot whose full width at half maximum is $\lambda/(2\,\mathrm{NA})$. The numerical aperture of the scanning system is $\mathrm{NA}=n\sin\theta$, the maximum angle of incidence is θ, and n is the real part of the refractive index. This is equivalent to Sparrow's criterion, in which diffraction limits the spatial resolution in a vacuum or air ($n=1$) to $\lambda/2$. Optical thermometry below the diffraction limit is based on near-field scanning optical microscopy (NSOM), which achieved resolution approaching 10 nm for optical imaging using a probe scanned a few nanometers above the surface. One NSOM method uses tapered, metal-coated optical fibers with an aperture at the tip [80]. Near-field infrared imaging used a tapered metal micropipette to collect infrared radiation emitted by a patterned metal bridge structure [81]. The fiber aperture was near 1.5 μm, which is almost an order of magnitude less than the dominant emitted wavelength at room temperature. Another technique delivered visible light through a metal-coated fiber with aperture near 50 nm [82]. The radiation reflected into the far field was used to image temperature differences between two metal bridges. For transient measurements, data interpretation was complicated by thermal expansion of the surface and probe. These exploratory scanning probe studies showed that the low transmittance through apertured probes ($\sim 10^{-6}$) can strongly limit the sensitivity for temperature measurements.

These problems may eventually be mitigated using solid immersion lens (SIL) technology, which improves spatial resolution as in oil immersion microscopy. Figure 12(*a*) indicates that a solid lens scanning in the near field can provide spatial resolution below the wavelength in air without the dramatic loss in transmission imposed by an apertured fiber. The plotted sixth-power dependence of transmission is based on the result of Bethe for apertures [83]. The SIL increases the numerical aperture of the optical path according to the real part of the refractive index of the lens material. The SIL with visible or ultraviolet radiation has achieved values of NA between 1.0 and 2.2 for optical imaging [84], data storage [85], and photolithography [86]. In principle, SILs with tailored optical properties should be appropriate for improving the spatial resolution of the various optical thermometry techniques described already in this section.

The first fully-micromachined silicon SIL [87] targeted near and mid-infrared radiation wavelengths, for which silicon is nearly transmitting with $n\sim 3.4$. Figure 12(*b*) shows the integrated silicon lens and cantilever. Lenses were fabricated by developing photoresist pillars on the silicon film on a silicon-on-insulator (SOI) substrate. The pillars were shaped into hemispheres during exposure to acetone vapor, and the shape was transferred into the silicon film using CF_4/O_2 reactive ion etching. Using transmission through a 1 μm aperture patterned in Cr/Au on a GaP substrate, the lens produced a spot size of $\lambda/5$ and $\mathrm{NA}=2.5$ with radiation wavelength $\lambda=9.3$ μm. Subsequent research imaged thermal radiation transmission through a micropatterned interconnect structure on silicon [88]. Figure 12(*c*) shows the improved resolution of the radiance images collected during a scan across two aluminum lines of width 1 μm and separated by 2.5 μm. Figure 12(*c*) is not a thermal map of the interconnect structure, but rather an image of the thermal radiation transmitted through the microstructure from an underlying heater, which shows that local measurements of temperature gradients should be possible. A

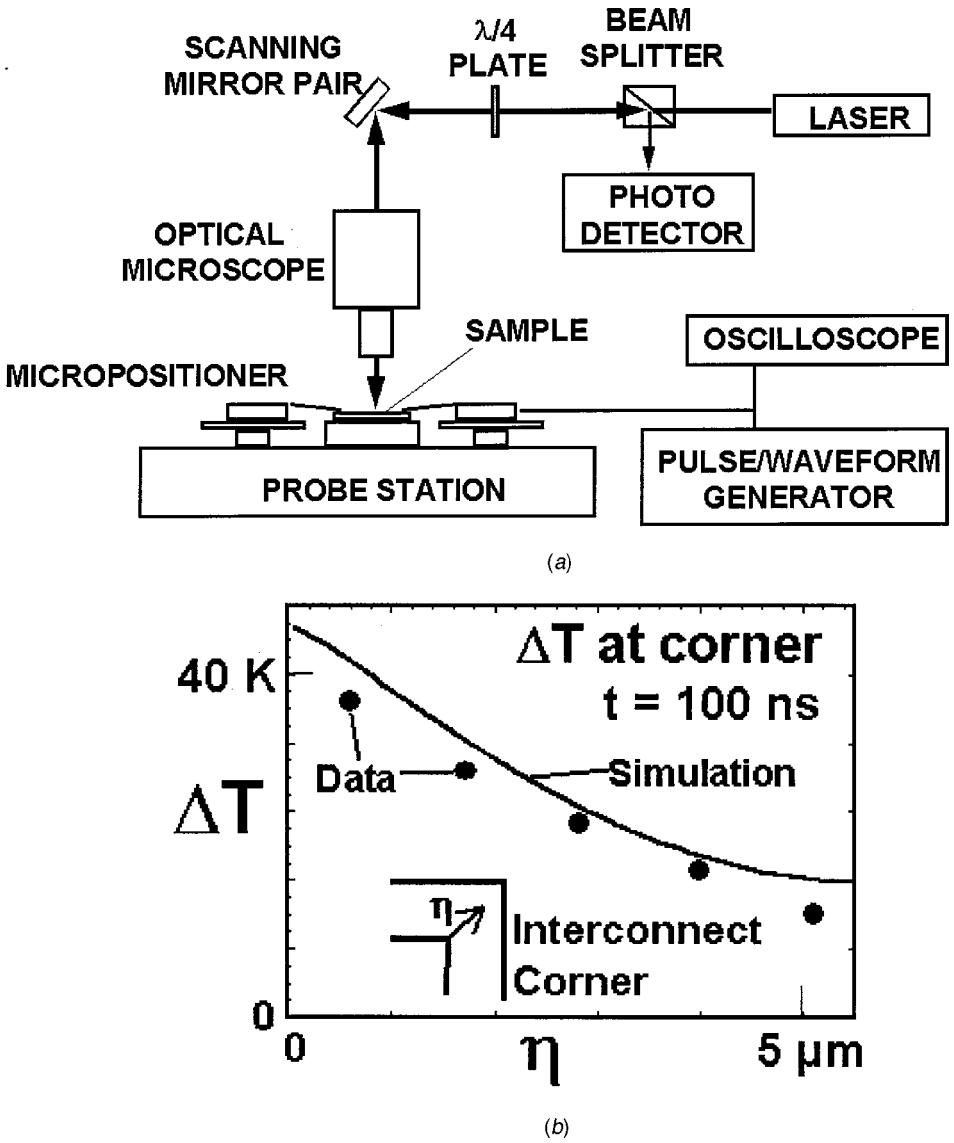

Fig. 11 (*a*) **Schematic of the setup for scanning laser-reflectance imaging of interconnects and semiconductor devices;** (*b*) **experimental data for the temperature distribution across the corner of an electrically heated metal intercorrect. For details see Refs. [62,76,77].**

noise equivalent temperature resolution below 0.2 K and a spatial resolution of 1.7 μm were predicted at 120°C using a diffraction-limited infrared microscope with InSb focal plane array detector at 20 Hz. Although the spatial resolution for optical microscopy may be improved through the use of a metal aperture patterned on the lens, the resulting reduction in optical transmittance and the noise-limited temperature sensitivity makes this approach unattractive for thermal imaging.

3 Thermal Transport in Low-Dimensional Structures

3.1 Thin Films. Thermal conduction in solid films can be strongly influenced by material imperfections and sub-continuum effects. The discrepancy between bulk and film thermal conductivities can in many cases be traced to imperfections or impurities introduced during the fabrication process. For single-crystal films of thickness comparable with the phonon mean free path, phonon-boundary scattering also reduces the effective thermal conductivity. Additional detail can be found in thin-film thermal conductivity reviews [89,90] and more focused articles on superlattices [91,92,93], interface resistance [94], diamond films [95,96], and organic films [97,98,99], and experimental methods [100].

3.1.1 Measurement Techniques. Thin film thermal conductivity measurement techniques are distinguished by the source and timescale of heating and the thermometry method. Many use electrical heating and thermometry in bridges patterned above the sample film. The 3ω method [101] sustains a current in a metal bridge at angular frequency ω, inducing fluctuations at 2ω of the heating rate and the temperature. The temperature amplitude and phase and the thermal properties of surrounding materials are extracted from the 3ω component of the voltage along the bridge. While the 3ω method first measured the out-of-plane thermal conductivity in dielectric films [102,103], recent extensions using multiple bridges of varying width measured the thermal conductivity anisotropy in superlattices [104], polyimide [105], and the in-plane conductivity of thin silicon films [106]. Measurements at heating frequencies up to 60 kHz yielded the volumetric heat capacity of silicon dioxide films [107]. Steady-state electrical heating and thermometry in parallel metal bridges is an alternative for determining film-substrate interface resistance [94] and the out-of-

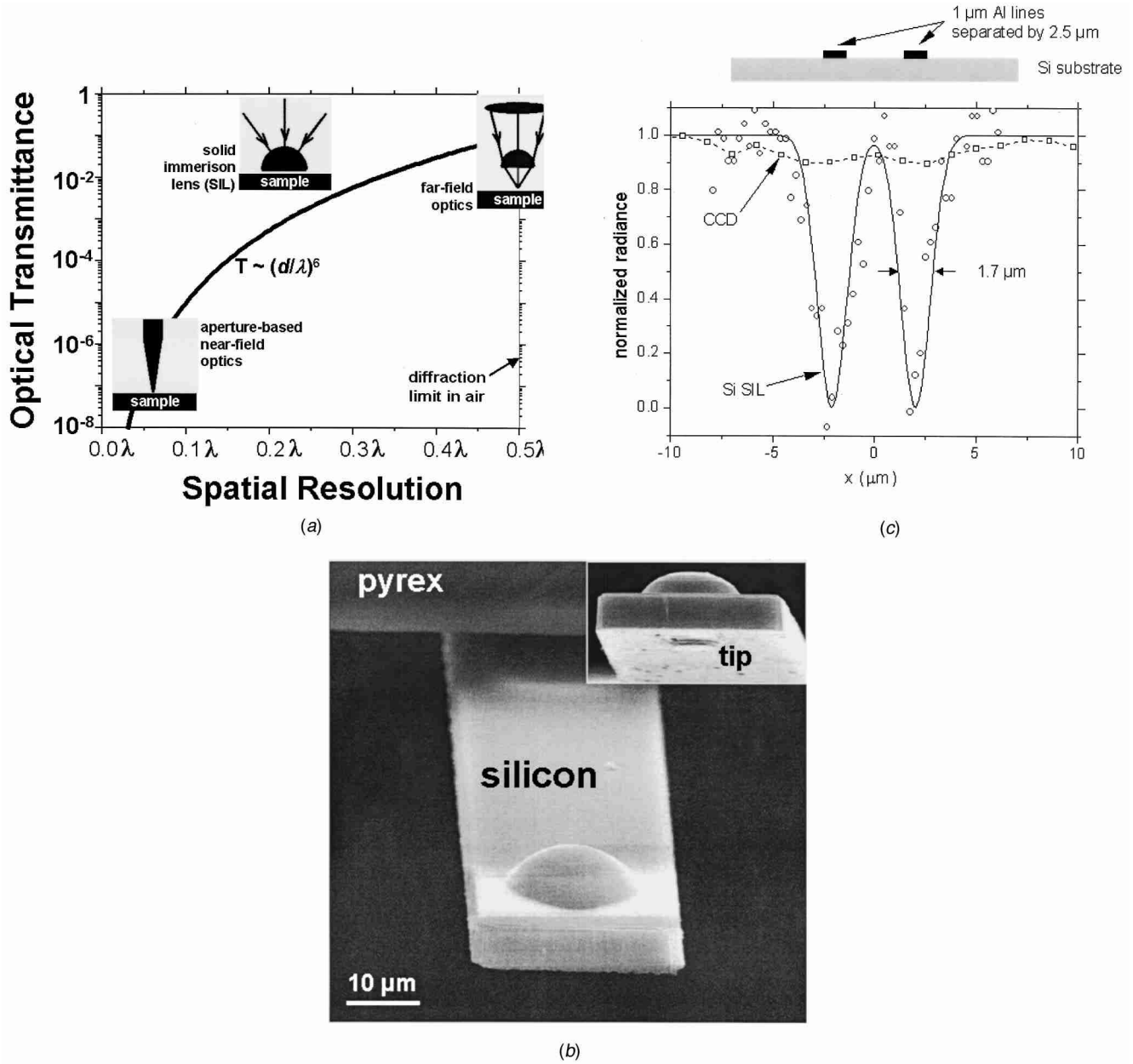

Fig. 12 (*a*) **Relationship of the transmittance and spatial resolution of optical imaging technologies, showing the promise of the solid immersion lens for thermal imaging. The curve plots the sixth power dependence of transmittance on diameter for a circular aperature.** (*b*) **Scanning electron micrograph of the silicon lens and tip and the pyrex mount.** (*c*) **Transmission data collected by an InSb CCD array through a patterned two-bridge structure with and without the SIL.**

plane thermal conductivities of disordered dielectric films [108]. Steady and transient heating in metal were used in membrane structures, generally fabricated using anisotropic chemical etching, to isolate the in-plane thermal conductivity [109,110,97].

Pulsed laser heating and thermoreflectance thermometry have been used for non-contact measurements of the out-of-plane conductivity. The instrumentation and analysis depends on the heating pulse duration. As discussed in section 2.2, measurements with picosecond-scale heating can examine transport in a variety of thin films and nanostructures. These measurements use pump-probe laser diagnostic to capture both the thermoreflectance response and the surface displacement resulting from acoustic waves. Analysis needs to consider the non-diffusive, sub-continuum nature of heat transport in the sample films and the disequilibrium between electrons, which can absorb much of the radiation, and the lattice. Nanosecond heating from a Nd:YAG laser and continuous time-domain laser-reflectance thermometry yielded the out-of-plane conductivities of silicon-dioxide [111] and polycrystalline diamond [112] films of thickness down to a few hundred nanometers. The lateral thermal conductivity of films on substrates has been measured using the transient thermal grating technique [113]. Pulsed laser radiation interferes on the sample surface, yielding a harmonic spatial variation of energy absorption. This yields spatially varying temperature and thermal strain fields, whose temporal decay is detected by the deflection of an incident probe beam. The temporal decay is governed mainly by the lateral thermal conductivity of the film and substrate and the volumetric heat capacity within a depth near the spatial period of energy deposition, which can be varied by altering the difference in incident angles between the two probes.

3.1.2 Single Crystal Films. The in-plane conductivities of single-crystal semiconducting monolayers are important for silicon-on-insulator (SOI) [114] and 3D circuits [115], as well as micromachined sensors and actuators involving crystalline silicon membranes [116]. Conduction is dominated by phonon transport, even for heavily-doped samples. Figure 13(*a*) shows that for nearly single-crystal silicon, phonon-interface scattering strongly reduces the effective thermal conductivity at low temperatures. The data can be predicted using the model of Holland [117] for conduction in silicon with modifications to account for scattering on film interfaces based on the phonon Boltzmann equation [118]. Crystalline monolayers are often bounded by amorphous films, which act as diffuse phonon emitter-absorbers owing to strong phonon scattering. When the mean free paths in neighboring films are comparable, which is the case in many superlattices, transport in the layers is coupled and the fraction of phonons specularly reflected must be determined from the interfacial roughness and the phonon wavelength. For single-crystal silicon layers doped at concentrations higher than 1.0×10^{17} cm^{-3} the conductivity is reduced by scattering on impurities and free electrons [119]. Figure 13(*a*) shows that this is particularly important at low temperatures. Measurements at 20 K on layers of thickness 3 μm with phosphorus and boron concentrations of 1.0×10^{18} cm^{-3} yielded reductions by approximately two and four, respectively, with the difference resulting from the disparity in mass of the two impurity types.

The anisotropy and nonlinearity of acoustic phonon dispersion relationships complicate predictions above 100 K for GaAs, Ge, and AlAs films, and above 200 K for silicon films owing to its higher Debye temperature. Figure 13(*b*) plots room-temperature in-plane thermal-conductivity data for silicon films in SOI substrates as thin as 74 nm [106]. The thermal conductivity is smaller by as much as 50 percent than the bulk value and decreases slowly with decreasing film thickness. A graybody approximation overpredicts the data because it neglects the spectral dependence of phonon scattering. Additional modeling lended support to the hypothesis that longitudinal phonons dominate transport. This hypothesis is consistent with the highly dispersive nature of high-frequency transverse acoustic phonons in silicon, which reduces their group velocities.

Epitaxially-grown high-temperature superconducting films, such as $YBa_2Cu_3O_7$, $EuBa_2Cu_3O_7$, and $BiSr_2Ca_1Cu_2O_8$, exhibit highly anisotropic thermal conduction properties due to their orthorhombic unit cell and the large density of oriented imperfections [120]. These films are promising for low-loss interconnects and Josephson junctions in hybrid superconductor/semiconductor circuits, as well as for thermal radiation detectors. Models have been developed for the conductivity reduction in films with the *c* axis oriented normal to the substrate [121,122]. These calculations considered the simultaneous contribution of electrons and phonons, because both carriers are significant at temperatures above a few tens of Kelvin.

The reduction is substantial for films thinner than about 100 nm and is dominated by the impact of interfaces on the phonon contribution. The electron thermal conductivity and associated thin-film size effect are strongly reduced at low temperatures due to the increasing concentration of Cooper pairs, which do not contribute to heat conduction.

3.1.3 Interfaces. In many cases, heat transport on short length-scales and time-scales is sensitive to the properties of interfaces. Thus, an ability to control and exploit interface thermal properties could enable improved thermal management of multilayer device structures [123], simplify the fabrication of thermal sensors, and increase the efficiency of thermoelectric energy conversion [124,125]. Furthermore, because thermal phonons near room temperature are sensitive to atomic-level structure, greater scientific understanding of heat transport at interfaces may lead to convenient, nondestructive methods for evaluating the microstructure of interfaces: interface microstructure is a critical issue in materials science but the high resolution electron microscopy and diffraction needed to characterize interface structure is often difficult, time-consuming and expensive.

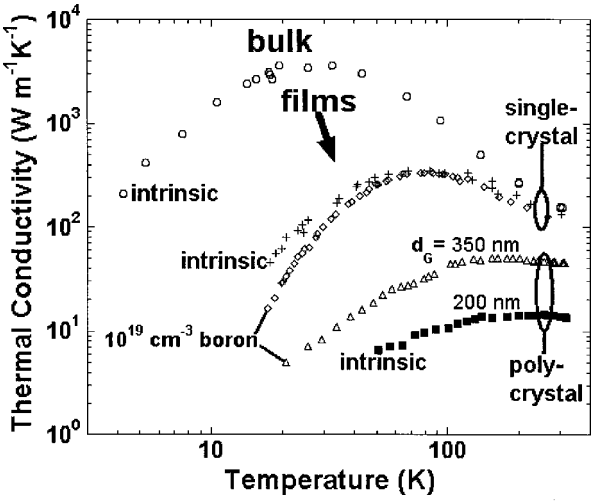

(*a*)

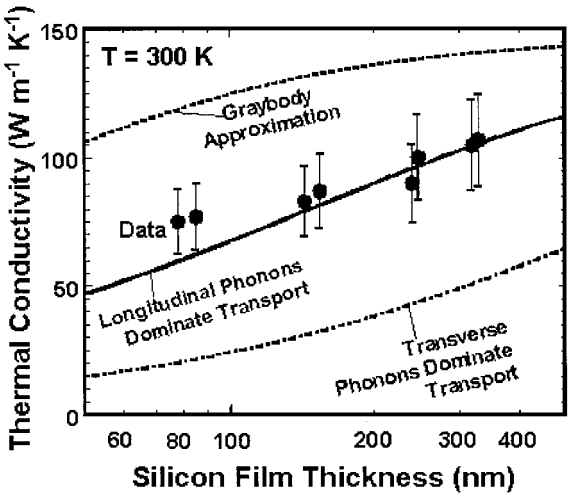

(*b*)

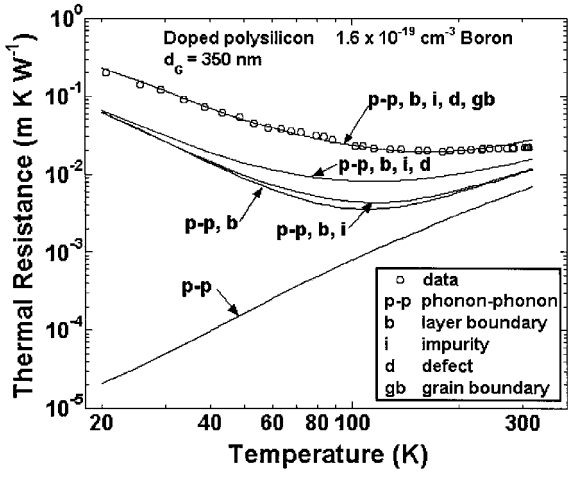

(*c*)

Fig. 13 (*a*) Data for bulk silicon compared with data for silicon single-crystal films and polysilicon. (*b*) Predictions and data for single-crystal silicon films of thickness down to 74 nm at room temperature as a function of film thickness. (*c*) Contributions to the thermal resistivity, 1/*k*, as a function of temperature for a doped polysilicon layer.

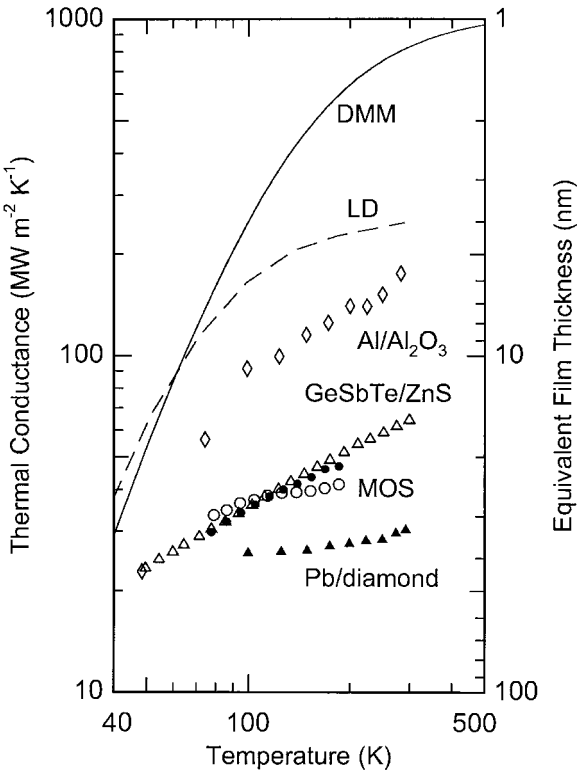

Fig. 14 Comparison of selected data for interface thermal conductance: (i) individual interfaces measured by picosecond thermoreflectance [52], Al/Al_2O_3 (open diamonds) and Pb/c-C (filled triangles); (ii) conductance of the a-$GeSbTe_{2.5}$/ZnS interface (open triangles) from a multilayer sample [133], (iii) series conductance of the top and bottom interfaces of metal-SiO_2-silicon structures (MOS, filled circles) [103]. The solid line is the calculated diffuse mismatch conductance of Al/Al_2O_3 using the Debye model; the dashed line is the theoretical prediction for Al/Al_2O_3 using a lattice-dynamical calculation of a model fcc interface [52]. The right axis gives the thickness of a film with $\Lambda = 1$ W m^{-1} K^{-1} that has the thermal conductance corresponding to the left axis.

3.1.3a Interface thermal conductance. We first consider the thermal conductance of an isolated interface, i.e., an interface that is separated from other interfaces by a distance that is large compared to the mean-free-path of the lattice vibrations that dominate heat transport in the material. In this limit, we can ignore coherent superposition of lattice waves reflected or transmitted by adjacent interfaces. The conductance of isolated interfaces has a long history in condensed matter physics beginning with the problem of the Kapitza conductance between a solid and liquid helium—an issue of great practical importance in the design of cryogenic refrigerators for low temperature physics. Swartz and Pohl [94] give an exhaustive review of thermal boundary resistance, the inverse of interface thermal conductance, through 1988.

Some recent data for interface thermal conductance are shown in Fig. 14. Surprisingly, near room temperature, the highest thermal conductance for metal/dielectric interfaces measured by picosecond thermoreflectance [52], Ti/Al_2O_3 and Al/Al_2O_3, is only a factor of ~5 larger than the lowest conductance, Pb/diamond. Other data for metal/dielectric interfaces [94,55,126,49], for the most part, fall between these two extremes. (Initial experiments on epitaxial TiN/MgO, however, indicate an interface conductance a factor of ~3 larger than Al/Al_2O_3, see Figs. 10 and 14.)

The diffuse mismatch model [94] provides a straightforward starting point for theoretical understanding of heat transport at an interface. The key assumption of this model is that phonons are randomly and elastically scattered at the interfaces with a transmission coefficient given by the relative density of vibrational states on the two sides of the interface [94,52,127]. Furthermore, if the Debye model is used for the density of states and mode dispersion, then the thermal conductance is easily calculated from the velocity of sounds and atomic densities of the two materials [94,127]. An example calculation using the diffuse mismatch model is shown in Fig. 14; this calculation for Al/Al_2O_3 overestimates the experimental data near room temperature by a factor of ≈5; if dispersion of the high energy vibrational modes is taken into account, the agreement improves [52].

The opposing limit is the assumption of no scattering at the interface; in the long-wavelength or continuum limit, phonon reflection and transmission is calculated from the mass density and anisotropic elastic constants of the materials. For shorter wavelengths, microscopic calculations of the lattice dynamics are needed; these models are typically based on idealized models of the interface structure and bonding [128,129]. The results of lattice-dynamical calculations [52] for Al/Al_2O_3, see Fig. 14, are in reasonably good agreement with the data.

While the data in Fig. 14 represent a significant advance, many more systematic studies will be needed to develop a comprehensive understanding; for example, experiments have not yet observed either the high or low extremes of conductance predicted by theory [52] and have not yet isolated contributions to heat transport at interfaces by anharmonicity, electron-phonon coupling [130], interface disorder [131] or altered interface bonding [132].

3.1.3b Multilayer thin films. Figure 14 also contains data for interface conductance extracted from studies of multilayers [133] and thin film samples [49,126] measured using the 3ω method. If the thermal conductivity of a thin layer of disordered material is independent of layer thickness d, i.e., if phonons with mean-free-paths comparable to d make a negligible contribution to heat transport, and that the microstructure of the thin layer is approximately independent of d, the measured conductance of a multilayer sample is the parallel sum of the thermal conductance of the individual layers and the thermal conductance of the interfaces [49,134,133]. Data for $GeSbTe_{2.5}$/ZnS interfaces (a component of phase-change data-storage media) nearly overlap with data for the series conductance of the metal/SiO_2 and SiO_2/Si interfaces of metal-oxide-semiconductor structures. These data for metallized SiO_2 layers on Si are in good agreement with previous room temperature measurements using nanosecond thermoreflectance [48].

While $GeSbTe_{2.5}$/ZnS multilayers show relatively small thermal conductance, our studies of multilayers of disordered oxides have failed to reveal a significant effect of interfaces: the thermal conductivity of ZrO_2:Y_2O_3/SiO_2 [135] and ZrO_2/Y_2O_3 [126] multilayers are almost independent of layer thickness with layer thickness as small as 4 nm. Apparently, the lattice vibrations of these oxides are sufficiently alike that the thermal conductance is too large to be measured by this approach. Multilayer coatings [136] do not, therefore, appear to be a promising route for lowering the conductivity of thermal barriers. Significant decreases in conductivity have been observed recently in nanocrystalline ZrO_2:Y_2O_3 [137] and attributed to the finite thermal conductance of grain boundaries.

3.1.3c Epitaxial superlattices. For a short-period superlattice with coherent interfaces, we must reevaluate our assumptions for isolated interfaces and consider superposition of lattice waves transmitted and reflected by the interfaces. Thermal transport in superlattices with perfect interfaces has been discussed in a series of papers using increasingly refined models of the lattice dynamics [138,139,140,141]. The general conclusion of this work is that a superlattice structure strongly reduces the average group velocity of phonons in the through-thickness direction and—because

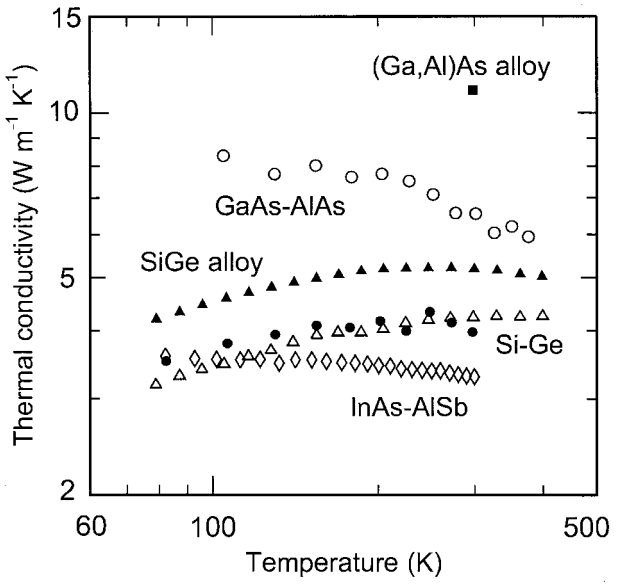

Fig. 15 Selected data for the through-thickness thermal conductivity of superlattices with bilayer periods of ≈ 5 nm; data for GaAs-AlAs (open circles, 5.67 nm period [54]) were measured by picosecond thermoreflectance; data for Si-Ge (open triangles, 5 nm period [142]; filled circles, 4.4 nm period [104]) and InAs-AlSb (open diamonds, 6.5 nm period [170]) were measured using the 3ω method. Data for $Si_{0.85}Ge_{0.15}$ [142] and $Ga_{0.4}Al_{0.6}As$ [144] alloys are included for comparison.

the thermal conductivity scales as the square of the group velocity—dramatically suppresses the thermal conductivity in comparison to the bulk components.

This suppression of thermal conductivity produced by zone-folding and phonon confinement cannot, however, fully explain the data, see Fig. 15. The observed reduction in conductivity is too large to be easily explained by the theories of perfect interfaces and both Si-Ge [142] and GaAs [54] superlattices show substantial decreases in conductivity with decreasing superlattice period; theory predicts that the conductivity should *increase* slowly with decreasing period [143].

Theory [93] based on incoherent (particle-like) scattering of phonons at interfaces predicts a superlattice thermal conductivity that decreases with superlattice period. Particle-based theory [93] can more easily explore effects of disorder but this approach requires approximations and assumptions concerning phonon dispersion, elastic vs. inelastic scattering, and specular vs. diffuse scattering that may be difficult to justify microscopically.

Interface disorder introduces diffuse scattering but disorder in a superlattice is typically modest and limited to interface roughness (a finite density of interface steps) and substitutional alloying at the interfaces caused by surface segregation during growth. Unfortunately, this physical and chemical interface roughness in an epitaxial superlattice is sensitive to the material, growth method, growth temperature, and deposition rate—and is notoriously difficult to characterize. Furthermore, asymmetry of the interface is often pronounced, i.e., the growth of component *A* on the surface of component *B* creates a different interface than the growth of *B* on *A*. Strained-layer superlattices such as Si-Ge can harbor high densities of crystalline defects when the layer thickness exceeds the critical thickness for the extension of misfit dislocations [104]; growth on relaxed buffer layers [104] reduces the density of threading dislocations but the misfit density will still be large when the critical thickness is exceeded.

Since the through-thickness conductivity of a short-period superlattice is smaller than the corresponding alloy [142,170], see Fig. 15, substitutional interface disorder acting alone is probably insufficient to explain the data. Approaches that combines both mechanisms, wave-interference and diffuse scattering [143], perhaps acting independently on different parts of the phonon spectrum, may be a more successful route to a microscopic theory. We note that emerging data on the anisotropy of superlattice thermal conductivity [145], i.e., the ratio of the in-plane to the through-thickness conductivity, may provide additional constraints on theoretical models.

3.1.4 Polycrystalline Films. In polycrystalline films, phonon scattering on grain boundaries and related defects dominates over boundary scattering. Doped polysilicon films are common in MEMS and as the gate terminal in silicon field-effect transistors. The grain structure and spatial impurity distribution depend strongly on the temperature and duration of annealing. Polysilicon conductivities are reduced compared to those of pure crystalline films [146], but the roles of impurities and grains are difficult to separate. Recent work studied films with grain sizes between 300 and 500 nm, extracted using transmission electron microscopy, and boron or phosphorus concentrations up to 4.1×10^{19} cm^{-3}, measured using secondary ion mass spectroscopy (SIMS) [147,148]. Figures 13(*a*) and 13(*c*) show that the conductivity is reduced strongly at all temperatures compared to similarly-doped single-crystal silicon layers, which illustrates the importance of grain boundary scattering. The data were predicted by reducing the mean free path using Matthiessen's rule [149] and a grain-boundary free path given by B/d_G, where d_G is the grain size and B is governed by the grain shape and grain boundary reflection coefficient. The data at 300 K are well approximated by

$$k(d_G,n)=\frac{1}{3}Cv\left(\frac{A_1}{d_G}+A_2n_i\right)^{-1},$$

where the phonon velocity and heat capacity are $v=6170$ m s^{-1} and $C=1.65\times10^6$ J m^{-3} K^{-1}, the grain size d_G has units of nm, and the impurity concentration n_i has units of cm^{-3}. The constant A_1 is 2.89×10^{10} m^2 and A_2 is 3.20×10^{-13} or -1.12×10^{-14} m^2 for boron and phosphorus, respectively.

For polycrystalline diamond films the orientation and minimum size of grains are governed by the details of the deposition process, in particular the nucleation technique, the substrate temperature, and the composition of the process gases. Verhoeven et al. [150] observed a particularly large degree of anisotropy for microwave CVD diamond films with predominantly heteroepitaxial grains, with the in-plane conductivity smaller by about one order of magnitude than the out-of-plane conductivity as shown in Fig. 16. The free path B/d_G is overly simplistic for diamond film data owing to the large concentration of other imperfections. Because imperfections populate primarily at grain boundaries, the phonon scattering rate can still be coupled to the grain size d_G. This concept was quantified using a dimensionless grain-boundary scattering strength [151], which is governed by the scattering cross sections and number density per unit grain boundary area of imperfections. For this model, the scattering rate is dictated by both the size of grains and the density of imperfections per unit grain boundary area.

3.1.5 Amorphous Oxide and Organic Films. For highly-disordered films, such as amorphous glasses and organic materials, the process-dependent material structure and stoichiometry influence the thermal conductivities and volumetric heat capacities. These films are common as passivation and thermal insulation in MEMS and integrated circuits. Silicon dioxide and silicon nitride films are often deposited at low temperatures to avoid diffusion or other failure mechanisms in micromachined structures. Lower deposition temperatures for silicon dioxide are known to reduce the mass density, which decreases the thermal conductivity [152] but increases the volumetric heat capacity owing to the large concentration of silanol [107]. Following a high-temperature anneal, the root-mean-square deviations of bond lengths, which can

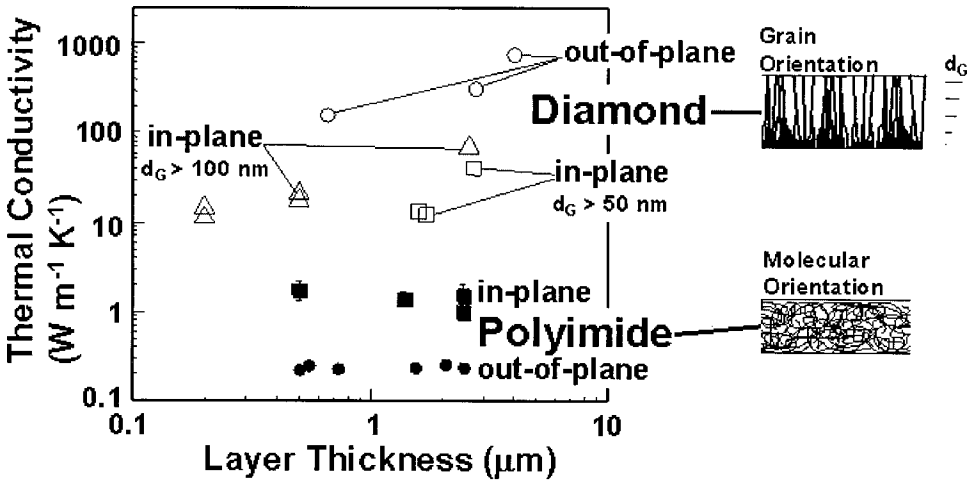

Fig. 16 The sketches indicate the impact of grain and molecular orientation on the anisotropy

serve as a measure of the degree of disorder, diminish considerably and approach those of thermally-grown silicon-dioxide films. The thermal properties of organic films are expected to be highly sensitive to their chemical composition and structural configuration. Figure 16 shows that polyimide films exhibit anisotropic conductivities due to the partial alignment of molecular strands in the film plane during spin coating. The modeling of heat conduction in disordered films is far more approximate than that of crystalline films, and is limited to estimates of the minimum conductivity [153] and simple models for the anisotropy of fully-amorphous stranded organic films [97].

3.2 Nanowires. Much of the past effort on synthesizing low-dimensional structures has focused on 0-D (quantum dots) [154] and two-dimensional (quantum wells and heterostructures) nanostructures. Except for carbon nanotubes [37], one-dimensional structures have received relatively little attention. This is mainly due to challenges in synthesis of single-crystal nanowires, which are important for determining structure-property relations. Recently, however, there have been some major advances in growth of monocrystalline semiconductor nanowires [155,156,157,158] and integrating them into devices [159,160,161]. While most of the current research is being focused on electronic and optical properties of nanowires [162], the manipulation of their thermoelectric properties through quantum confinement of electrons is extremely promising for developing solid-state energy conversion devices [46]. In this case, one must study thermal transport in these nanowires as well, which can be very different from those of bulk materials. For example, Schwab et al. [163] observed quantum thermal conductance in nanofabricated one-dimensional nanostructures, where the quantum of phonon conductance is $g_o = \pi^2 k_B^2 T/(3h)$, where k_B is the Boltzmann constant, T is the temperature, and h is the Planck constant. In this regime, a one-dimensional nanostructure behaves essentially like a phonon waveguide similar to optical ones for light. Phonon transport in nanowire can be different from that in bulk semiconductors mainly because the dispersion relation could be significantly modified due to confinement in two directions. In addition, the presence of a surface can introduce surface phonon modes. These result in many different phonon polarizations other than the two transverse and one longitudinal acoustic branches found in bulk semiconductors. Such changes in the dispersion relation can modify the group velocity and the density of states of each branch. The phonon lifetime also changes and this arises from two sources. First, the phonon-phonon interactions can change because selection rules based on energy conservation and wavevector relations depend on the dispersion relation. Second, boundary scattering can be much stronger in nanowires (5–50 nm diameter) than in bulk semiconductors [164]. While there have been some theoretical studies on phonon conduction in nanowires [165,166], experiments have lagged behind. Recently, there have been some attempts [167] to measure the thermal conductivity of a collection or a mat of carbon nanotubes. However, due to weak coupling between carbon nanotubes, the actual thermal conductivity was found to be much lower than that predicted [168]. To accurately measure thermal properties of nanowires and compare them with theoretical studies, one must develop techniques to study the thermal behavior of isolated nanowires.

Figure 17 shows a micromachined structure that was developed by Shi [33,169]. The device is a suspended structure consisting of two adjacent silicon nitride (SiN_x) membranes or islands suspended with three 200 μm long and 2 μm wide silicon nitride beams. One 30 nm thick, 200 nm wide, and 150 μm long plati-

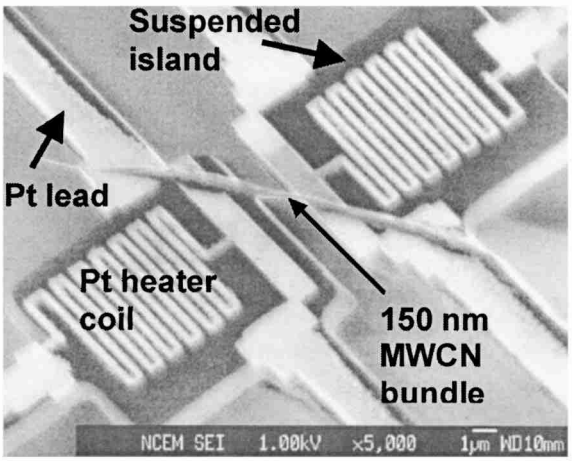

Fig. 17 Electron micrograph of the suspended heater structure used for measuring thermal conductivity of nanowires. Also laid across the heater is a multiwall carbon nanotube bundle 150 nm in diameter. The Pt heater coil on one of the suspended islands is heated and its temperature is measured by resistance thermometry. The temperature of the other island increases due to conduction through the nanowire, which is also measured by resistance thermometry. The temperature difference for a known heat flow rate from the heated island can be used to estimate the thermal conductivity of the nanowire.

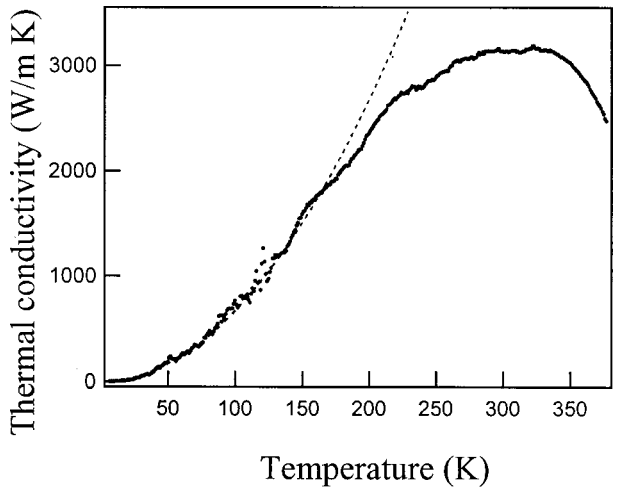

Fig. 18 Temperature dependence of thermal conductivity of a multiwall carbon nanotube. The dashed line corresponds to a T^2 temperature dependence. The thermal conductivity is about 3000 W/m-K at room temperature, which includes the contact resistances at the two islands.

num (Pt) heater/thermometer coil is built on each island. A nanowire can be placed in between and bridge the two suspended islands by several methods. A general method is to deposit a drop of aqueous solution containing nanotubes and nanowires on a wafer with densely packed suspended structures. This method has been successfully used to place SWCNs or MWCNs on the suspended structures. In the case of SWCN, nanotubes can also be grown between two islands using chemical vapor deposition (CVD). For this method, catalyst particles consisting of Fe, Al_2O_3, and Mo are first deposited on the islands from aqueous solution. Then the device is placed in a 750–900°C CVD chamber with methane gas flow. There is a good chance that one or several SWCNs can be grown and bridging the two islands.

To measure the thermal conductivity, one of the islands is heated to a temperature, T_h, which is determined by measuring the resistance of the Pt wire on the island. Conduction through the nanowire heats the sensing island to a temperature T_s, which is also measured by resistance thermometry. By noting the power dissipated by the heater, Q_h, and estimating the thermal conductance of the suspended legs connecting the islands in the absence of a nanowire, the conductance of the nanowire G_n can be calculated in a vacuum environment. Figure 18 shows the plot of thermal conductivity of a multiwall carbon nanotube as a function of temperature measured by this technique. The T^2 temperature dependence suggests that MWCN thermally behaves like a two-dimensional solid and has a thermal conductivity of about 3000 W/m-K at room temperature. This is approximately half of what is theoretically predicted [168]. Note that the measured value includes the contact resistance between the nanotube and the two islands, although it is predicted to be lower than the resistance of the tube itself [169]. Estimation of the contact resistance has remained a challenge. Nevertheless, it is envisioned that this technique can be used to measure thermal conductivities of a variety of semiconducting or metallic nanowires that are of technological importance.

4 Closing Remarks

This paper provides a critical review of two interrelated areas of research, namely, microscale thermometry and thermal transport in solid micro/nanostructures. The technology for measuring temperature and studying thermal transport is sufficiently advanced that one can now approach scales on the order of the mean free path and relaxation times of electrons and phonons at room temperature. The underlying principles, recent advances, and future challenges and research directions of scanning thermal microscopy, picosecond thermoreflectance, and scanning optical thermometry are discussed here. Experiments based on these techniques have led to fundamental understanding of electron, phonon and photon interactions and transport in both bulk and micro/nanostructured solids as well as solid-state devices. While these techniques are being developed to study thermal phenomena at microscales, it is clear that a fundamental understanding of microscale heat transfer is necessary to make further advances in these techniques. Much work remains to be done for further refining and combining these techniques. For example although one can now study short length and time scales thermal phenomena independently, it is currently very difficult to study thermal phenomena at small length and time scales simultaneously. In addition, although significant advances have occurred over the past decade, these techniques are limited to only a few laboratories. There needs to be more effort in making these techniques sufficiently robust and accessible so that the barrier for researchers to enter this field is greatly reduced.

This paper presents a critical review of thermal transport in two-dimensional and one-dimensional solid microstructures. In particular, phonon transport in single crystal, polycrystalline, and amorphous oxide and organic thin films is elucidated. The role of interfaces in multilayered polycrystalline and epitaxial thin films is also discussed. Finally, thermal transport in carbon nanotubes is presented and the opportunities for further research on nanowires are explored. For single crystal films, the effect of film thickness on thermal conductivity in materials such as Si is now fairly well understood and the thermal conductivities can be predicted using Boltzmann transport theory. For other materials, however, the non-linearity of the acoustic phonon dispersion relations makes it difficult to predict thermal conductivities at room temperature. In fact, in many materials the contribution of each phonon branch, longitudinal and transverse, to the thermal conductivity is largely unknown. For polycrystalline Si and diamond films, grain boundary scattering has been found to strongly reduce thermal conductivity. The value depends on the grain structure, which in turn depends on the growth process. Thermal properties of organic films are very sensitive to the chemical composition and structural configuration. For example, spin coating a polyimide film partially aligns the polymer chains along the film plane, which produces anisotropic thermal conductivity. Simple models have been developed to predict their thermal conductivity although detailed models based on fundamental understanding of polymer structure and chemistry remains to be developed.

Thermal transport across solid-solid interfaces remains one of the most challenging problems. While acoustic and diffuse mismatch models have been developed, their predictions rarely agree with experimental data. These models are phenomenological and do not isolate contributions to heat transport by anharmonicity, electron-phonon coupling, interfacial disorder and chemistry. Experiments have shown that interfaces play a very important role in epitaxial superlattices, where interface roughness and alloying introduces phonon scattering and thereby reduces the effective thermal conductivity. In some cases, it has been found that the thermal conductivity reduction exceeds even that offered by a collection of individual interfaces. It is conjectured that the wave interference from multiple interfaces, which produces phonon bandgaps and thereby reduction of group velocity, may play an important role. However, what is clear is that fundamental understanding of the individual and collective role of interfaces on thermal conductivity is largely missing.

While most of the paper discusses thermal transport in two-dimensional confined structures (films), it briefly discusses phonon transport in one-dimensional nanostructures, such as carbon nanotubes. It is expected that these and other nanowires are likely

to play an important role in nanostructured materials and devices, and therefore ought to be thermally studied. Confinement in an additional dimension might offer avenues of pushing the thermal conductivity to the extremes, as exemplified in carbon nanotubes. However, theoretical and experimental studies in this area have only just begun, and much remains to be understood.

Acknowledgments

DGC was supported by NSF Grant No. CTS 99-78822 and the U.S. Department of Energy, Division of Materials Sciences under Award No. DEFG02-ER9645439, through the Frederick Seitz Materials Research Laboratory at the University of Illinois at Urbana-Champaign. Picosecond thermoreflectance measurements and film thickness characterization used the Laser Facility and the Center for Microanalysis of Materials, University of Illinois. DGC thanks K. E. O'Hara (Integrated Micromachines) for invaluable assistance with the picosecond experiments and H. J. Maris, G. Chen, P. M. Norris, and G. D. Mahan for helpful discussions.

KEG appreciates the help of D. A. Fletcher and A. D. McConnell of Stanford University in preparing the sections on the SIL and polysilicon films, respectively. KEG also appreciates the many technical contributions of former students including M. Asheghi of Carnegie Mellon University, K. Kurabayashi of The University of Michigan, Y. S. Ju of IBM Corporation, M. N. Touzelbaev of AMD, and P. G. Sverdrup of Intel Corporation. Sponsorship was provided from the SRC through tasks 751 and 754.

AM greatly appreciates the support of the NSF, the DOE (Engineering Division, Basic Energy Sciences), and DARPA for their support. AM acknowledges the many contributions of several former students and post-docs, in particular, Jie Lai (Microsemi Corp.), Ke Luo (TriQuint Semiconductor), Madhavi Chandrachood (Applied Materials), Osamu Nakabeppu (Keio Univ.), John Varesi (Raytheon), and Li Shi (IBM Research Division). He also thanks Paul McEuen, Sergie Plyasunov, Adrian Bachtold and Philip Kim (Physics, UCB) for their help with nanotube related research.

Nomenclature

D = thermal diffusivity
f = modulation frequency of the probe beam
G = interface thermal conductance (per unit area)
k = imaginary part of the complex index of refraction
l = thermal diffusion length
$\tilde{n}$ = complex index of refraction
q = summation index
$\Delta R_1(t)$ = change in optical reflectivity at time t following a single pump pulse
t = time
T = temperature
$\Delta T_1(t)$ = temperature excursion at time t following a single pump pulse
$\Delta T(\nu)$ = frequency domain temperature response
V_{LI} = lock-in signal expressed as a complex number
V_{in} = in-phase lock-in signal
V_{out} = out-of-phase lock-in signal
λ = laser wavelength ($\approx$800 nm for Ti:sapphire)
ν = frequency
τ = time between mode-locked optical pulses

References

[1] Verhoeven, H., Boettger, E., Flöter, A., Reiss, H., and Zachai, R., 1997, "Thermal Resistance and Electrical Insulation of Thin Low-Temperature-Deposited Diamond Films," Diamond Relat. Mater., **6**, pp. 298–302.
[2] Banerjee, K., Amerasekera, A., Dixit, G., Cheung, N., and Hu, C., 1997, "Characterization of Contact and Via Failure under Short Duration Hight Pulsed Current Stree," *Proc. International Reliability Physics Symposium*, pp. 216–220.
[3] Cheung, N. K., Nosu, K., and Winzer, G., 1990, "Guest Editorial—Dense Wavelength Division Multiplexing Techniques for High Capacity and Multiple Access Communication Systems," IEEE J. Sel. Areas Commun., **8**, pp. 945–947.
[4] Margalit, N. M., Babic, D. I., Streubel, K., Mirin, R. P., Mars, D. E., Bowers, J. E., and Hu, E. L., 1996, "Laterally Oxidized Long Wavelength CW Vertical Cavity Lasers," Appl. Phys. Lett., **69**, pp. 471–473.
[5] Karim, A., Bjorlin, S., Piprek, J., and Bowers, J. E., 2000, "Long-Wavelength Vertical Cavity Lasers and Amplifiers," IEEE J. Sel. Top. Quantum Electron., **6**, pp. 1244–1253.
[6] Towe, E., Leheny, R. F., and Yang, A., 2000, "A Historical Perspective of the Development of the Vertical-Cavity Surface Emitting Laser," IEEE J. Sel. Top. Quantum Electron., **6**, pp. 1458–1464.
[7] Fan, X. F., Zeng, G. H., LaBounty, C., Bowers, J. E., Croke, E., Ahn, C. C., Huxtable, S., Majumdar, A., and Shakouri, A., 2001, "SiGeC/Si Superlattice Coolers," Appl. Phys. Lett., **78**, pp. 1580–1582.
[8] Mahan, G., Sales, B., and Sharp, J., 1997, "Thermoelectric Materials: New Approaches to an Old Problem," Phys. Today, **50**, pp. 42–47.
[9] Dresselhaus, M. S., Dresselhaus, G., Sun, X., Zhang, Z., Cronin, S. B., Koga, T., Ying, J. Y., and Chen, G., 1999, "The Promise of Low-Dimensional Thermoelectric Materials," Microscale Thermophys. Eng., **3**, pp. 89–100.
[10] Williams, C. C., and Wickramasinghe, H. K., 1986, "Scanning Thermal Profiler," Appl. Phys. Lett., **49**, pp. 1587–1589.
[11] Williams, C. C., and Wickramasinghe, H. K., 1988, "Photothermal Imaging With Sub-100 nm Spatial Resolution," in *Optical Sciences*, A. L. Schawlow, ed. Springer Series, pp. 364–369.
[12] Majumdar, A., Carrejo, J. P., and Lai, J., 1993, "Thermal Imaging Using the Atomic Force Microscope," Appl. Phys. Lett., **62**, pp. 2501–2503.
[13] Majumdar, A., Lai, J., Chandrachood, M., Nakabeppu, O., Wu, Y., and Shi, Z., 1995, "Thermal Imaging by Atomic Force Microscopy Using Thermocouple Cantilever Probes," Rev. Sci. Instrum., **66**, pp. 3584–3592.
[14] Stopka, M., Hadjiiski, L., Oerterschulze, E., and Kassing, R., 1995, "Surface Investigations by Scanning Thermal Microscopy," J. Vac. Sci. Technol. B, **13**, pp. 2153–2156.
[15] Luo, K., Shi, Z., Lai, J., and Majumdar, A., 1996, "Nanofabrication of Sensors on Cantilever Probe Tips for Scanning Multiprobe Microscopy," Appl. Phys. Lett., **68**, pp. 325–327.
[16] Oesterschulze, E., Stopka, M., Ackermann, L., Scholz, W., and Werner, S., 1996, "Thermal Imaging of Thin Films by Scanning Thermal Microscope," J. Vac. Sci. Technol. B, **14**, pp. 832–837.
[17] Luo, K., Shi, Z., Varesi, J., and Majumdar, A., 1997, "Sensor Nanofabrication, Performance, and Conduction Mechanisms in Scanning Thermal Microscopy," J. Vac. Sci. Technol. B, **15**, pp. 349–360.
[18] Nakabeppu, O., Igeta, M., and Hijikata, K., 1997, "Experimental Study of Point Contact Transport Phenomena Using the Atomic Force Microscope," Microscale Thermophys. Eng., **1**, pp. 201–213.
[19] Mills, G., Zhou, H., Midha, A., Donaldson, L., and Weaver, J. M. R., 1998, "Scanning Thermal Microscopy Using Batch Fabricated Thermocouple Probe," Appl. Phys. Lett., **72**, pp. 2900–2902.
[20] Nonnenmacher, M., and Wickramasinghe, H. K., 1992, "Scanning Probe Microscopy of Thermal Conductivity and Substrate Properties," Appl. Phys. Lett., **61**, pp. 168–170.
[21] Pylkki, R. J., Moyer, P. J., and West, P. E., 1994, "Scanning Near-Field Optical Microscopy and Scanning Thermal Microscopy," Jpn. J. Appl. Phys., Part 1, **33**, pp. 3785–3790.
[22] Maywald, M., Pylkki, R. J., and Balk, L. J., 1994, "Imaging of Local Thermal and Electrical Conductivity With Scanning Force Microscopy," Scanning Microsc., **8**, pp. 181–188.
[23] Hammiche, A., Hourston, D. J., Pollock, H. M., Reading, M., and Song, M., 1996, "Scanning Thermal Microscopy: Sub-Surface Imaging, Thermal Mapping of Polymer Blends, and Localized Calorimetry," J. Vac. Sci. Technol. B, **14**, pp. 1486–1491.
[24] Hammiche, A., Reading, M., Pollock, H. M., Song, M., and Hourston, D. J., 1996, "Localized Thermal Analysis Using a Miniaturized Resistive Probe," Rev. Sci. Instrum., **67**, pp. 4268–4273.
[25] Nakabeppu, O., Chandrachood, M., Wu, Y., Lai, J., and Majumdar, A., 1995, "Scanning Thermal Imaging Microscopy Using Composite Cantilever Probes," Appl. Phys. Lett., **66**, pp. 694–696.
[26] Varesi, J., and Majumdar, A., 1998, "Scanning Joule Expansion Microscopy at Nanometer Scales," Appl. Phys. Lett., **72**, pp. 37–39.
[27] Majumdar, A., and Varesi, J., 1998, "Nanoscale Temperature Distributions Measured by Scanning Joule Expansion Microscopy," ASME J. Heat Transfer, **120**, pp. 297–305.
[28] Binnig, G., Quate, C. F., and Gerber, Ch., 1986, "Atomic Force Microscope," Phys. Rev. Lett., **56**, pp. 930–933.
[29] Lai, J., Chandracood, M., Majumdar, A., and Carrejo, J. P., 1995, "Thermal Detection of Device Failure by Atomic Force Microscopy," IEEE Electron Device Lett., **16**, pp. 312–315.
[30] Luo, K., Herrick, R. W., Majumdar, A., and Petroff, P., 1997, "Scanning Thermal Microscopy of a Vertical Cavity Surface Emitting Laser," Appl. Phys. Lett., **71**, pp. 1604–1606.
[31] Ruiz, F., Sun, W. D., Pollak, F. H., and Venkatraman, C., 1998, "Determination of Thermal Conductivity of Diamond-Like Nanocomposite Films Using a Scanning Thermal Microscope," Appl. Phys. Lett., **73**, pp. 1802–1804.
[32] Majumdar, A., 1999, "Scanning Thermal Microscopy," Annu. Rev. Mater. Sci., **29**, pp. 505–585.
[33] Shi, L., 2001, "Mesoscopic Thermophysical Measurements of Microstructures and Carbon Nanotubes," Ph.D. thesis, Dept. of Mechanical Engineering, UC Berkeley.

[34] Shi, L., Kwon, O., Miner, A. C., and Majumdar, A., 2001, ''Design and Fabrication of Probes for Sub-100 nm Scanning Thermal Microscopy,'' J. of MEMS, **10**, pp. 370–378.
[35] Shi, L., and Majumdar, A., ''Thermal Transport Mechanisms at Nanoscale Point Contacts,'' ASME J. Heat Transfer (in press).
[36] Kwon, O., 2001, ''Thermal Design, Fabrication, and Imaging of MEMS and Microelectronic Structures,'' Ph.D. dissertation, Dept. of Mechanical Engineering, U.C. Berkeley.
[37] Dresselhaus, M. S., Dresselhaus, G., and Eklund, P., 1996, *Science of Fullerenes and Carbon Nanotubes*, Academic Press, New York.
[38] Shi, L., Plyasunov, S., Bachtold, A., McEuen, P., and Majumdar, A., 2000, ''Scanning Thermal Microscopy of Carbon Nanotubes Using Batch Fabricated Probes,'' Appl. Phys. Lett., **77**, pp. 4295–4297.
[39] Yao, Z., Kane, C. L., and Dekker, C., 2000, ''High-Field Electric Transport in Single-Wall Carbon Nanotubes,'' Phys. Rev. Lett., **84**, pp. 2941–2944.
[40] Phelan, P. E., Nakabeppu, O., Ito, K., Hijikata, K., Ohmori, T., and Torikoshi, K., 1993, ''Heat Transfer and Thermoelectric Voltage at Metallic Point Contacts,'' ASME J. Heat Transfer, **115**, pp. 757–762.
[41] Loomis, J. J., and Maris, H. J., 1994, ''Theory of Heat Transfer by Evanescent Electromagnetic Waves,'' Phys. Rev. B, **50**, pp. 18517–18524.
[42] Xu, J. B., Lüger, K., Möller, R., Dransfeld, K., and Wilson, I. H., 1994, ''Heat Transfer Between Two Metallic Surface at Small Distances,'' J. Appl. Phys., **76**, pp. 7209–7216.
[43] Mulet, J. P., Joulian, K., Carminati, R., and Greffet, J. J., 2001, ''Nanoscale Radiative Heat Transfer Between a Small Particle and a Plane Surface,'' Appl. Phys. Lett., **78**, pp. 2931–2933.
[44] Leinhos, T., Stopka, M., and Oesterschulze, E., 1998, ''Micromachined Fabrication of Si Cantilevers With Schottky Diodes Integrated in the Tip,'' Appl. Phys. A: Solids Surf., **66**, pp. S65–S69.
[45] Mihalcea, C., Vollkopf, A., and Oesterschulze, E., 2000, ''Reproducible Large-Area Microfabrication of Sub-100 nm Apertures on Hollow Tips,'' J. Electrochem. Soc., **147**, pp. 1970–1972.
[46] Hicks, L. D., and Dresselhaus, M. S., 1993, ''Thermoelectric Figure of Merit of a One-Dimensional conductor,'' Phys. Rev. B, **47**, pp. 16631–16634.
[47] Paddock, C. A., and Eesley, G. L., 1986, ''Transient Thermoreflectance From Thin Metal Films,'' J. Appl. Phys., **60**, pp. 285–290.
[48] Käding, O. W., Skurk, H., and Goodson, K. E., 1994, ''Thermal Conductance in Metallized Silicon-Dioxide Layers on Silicon,'' Appl. Phys. Lett., **65**, pp. 1629–1631.
[49] Lee, S.-M., and Cahill, D. G., 1997, ''Heat Transport in Thin Dielectric Films,'' J. Appl. Phys., **81**, pp. 2590–2595.
[50] Hostetler, J. L., Smith, A. N., Czajkowsky, D. M., and Norris, P. M., 1999, ''Measurement of the Electron-Phonon Coupling Factor Dependence on Film Thickness and Grain Size in Au, Cr, and Al,'' Appl. Opt., **38**, pp. 3614–3620.
[51] Clemens, B. M., Eesley, G. L., and Paddock, C. A., 1988, ''Time-Resolved Thermal Transport in Compositionally Modulated Metal Films,'' Phys. Rev. B, **37**, pp. 1085–1096.
[52] Stoner, R. J., and Maris, H. J., 1993, ''Kapitza Conductance and Heat Flow Between Solids at Temperatures From 50 to 300 K,'' Phys. Rev. B, **48**, pp. 16373–16387.
[53] Taketoshi, N., Baba, T., and Ono, A., 1999, ''Observation of Heat Diffusion Across Submicrometer Metal Thin Films Using a Picosecond Thermoreflectance Technique,'' Jpn. J. Appl. Phys., Part 2, **38**, pp. L1268–1271.
[54] Capinski, W. S., Maris, H. J., Ruf, T., Cardona, M., Ploog, K., and Katzer, D. S., 1999, ''Thermal-Conductivity Measurements of GaAs/AlAs Superlattices Using a Picosecond Optical Pump-and-Probe Technique,'' Phys. Rev. B, **59**, pp. 8105–8113.
[55] Smith, A. N., Hostetler, J. L., and Norris, P. M., 2000, ''Thermal Boundary Resistance Measurements Using a Transient Thermoreflectance Technique,'' Microscale Thermophys. Eng., **4**, pp. 51–60.
[56] Capinski, W. S., and Maris, H. J., 1996, ''Improved Apparatus for Picosecond Pump-and-Probe Optical Measurements,'' Rev. Sci. Instrum., **67**, pp. 2720–2726.
[57] Bonello, B., Perrin, B., and Rossignol, C., 1998, ''Photothermal Properties of Bulk and Layered Materials by the Picosecond Acoustics Technique,'' J. Appl. Phys., **83**, pp. 3081–3088.
[58] Carslaw, H. S., and Jaeger, J. C., 1959, *Conduction of Heat in Solids*, Oxford University Press, New York, pp. 109–112.
[59] Chen, G., and Tien, C. L., 1993, ''Internal Reflection Effects on Transient Photothermal Reflectance,'' J. Appl. Phys., **73**, pp. 3461–3466.
[60] Mertin, W., 1996, ''New Aspects in Electro-Optic Sampling,'' Microelectron. Eng., **31**, pp. 365–376.
[61] Sheridan, J. A., Bloom, D. M., and Solomon, P. M., 1995, ''System for Direct Measurement of the Step Response of Electronic Devices on the Picosecond Time-Scale,'' Opt. Lett., **20**, pp. 584–586.
[62] Ju, Y. S., and Goodson, K. E., 1999, *Microscale Heat Conduction in Integrated Circuits and Their Constituent Films*, chap. 2, Kluwer Academic Publishers, Norwell, MA.
[63] Brugger, H., and Epperlein, P. W., 1990, ''Mapping of Local Temperatures on Mirrors of GaAs/AlGaAs Laser Diodes,'' Appl. Phys. Lett., **56**, pp. 1049–1051.
[64] Ostermeier, R., Brunner, K., Abstreiter, G., and Weber, W., 1992, ''Temperature Distribution in Si-MOSFET's Studied by Micro-Ramn Spectroscopy,'' IEEE Trans. Electron Devices, **39**, pp. 858–863.
[65] Iwata, K., and Hamaguchi, H., 1997, ''Microscopic Mechanism of Solute-Solvent Energy Dissipation Probed by Picosecond Time-Resolved Raman Spectroscopy,'' J. Phys. Chem., **101**, No. 4, pp. 632–637.
[66] Martin, Y., and Wickramsinghe, H. K., 1987, ''Study of Dynamic Current Distribution in Logic Circuits by Joule Expansion Microscopy,'' Appl. Phys. Lett., **50**, pp. 167–168.
[67] Donnelly, V. M., 1993, ''Extension of Infrared-Laser Interferometric Thermometry to Silicon-Wafers Polished on Only One Side,'' Appl. Phys. Lett., **63**, No. 10, pp. 1396–1396.
[68] Glanner, G. J., Sitter, H., Faschinger, W., and Herman, M. A., 1994, ''Evaluation of Growth Temperature, Refractive-Index, and Layer Thickness of Thin znte, mnte, and cdte-films by in-situ Visible Laser Interferometry,'' Appl. Phys. Lett., **65**, No. 8, pp. 998–1000.
[69] Hall, D. C., Goldberg, L., and Mehuys, D., 1992, ''Technique for Lateral Temperature Profiling in Optoelectronic Devices Using a Photoluminescence Microscope,'' Appl. Phys. Lett., **61**, pp. 384–386.
[70] Kolodner, P., and Tyson, J. A., 1982, ''Microscopic Fluorescent Imaging of Surface Temperature Profiles with 0.01 C Resolution,'' Appl. Phys. Lett., **40**, pp. 782–784.
[71] Cardona, M., 1969, ''Modulation Spectroscopy,'' in *Solid State Physics*, Suppl. 11, F. Seitz, D. Turnbull, and H. Ehrenreich, eds., Acadmic Press, New York.
[72] Claeys, W., Dilhaire, S., Quintard, V., Dom, J. P., and Danto, Y., 1993, ''Thermoreflectance Optical Test Probe for the Measurement of Current-Induced Temperature Change in Microelectronic Components,'' Reliability Engineering International, **9**, pp. 303–308.
[73] Mansanares, A. M., Roger, J. P., Fournier, D., and Boccara, A. C., 1994, ''Temperature Field Determination of InGaAsP/InP Lasers by Photothermal Microscopy: Evidence for Weak Nonradiative Process at the Facets,'' Appl. Phys. Lett., **64**, pp. 4–6.
[74] Epperlein, P.-W., 1993, ''Micro-Temperature Measurements on Semiconductor Laser Mirrors by Reflectance Modulation: A Newly Developed Technique for Laser Characterization,'' Jpn. J. Appl. Phys., Part 1, **32**, pp. 5514–5522.
[75] Abid, R., Miserey, F., and Mezroua, F.-Z., 1996, ''Effet de la temperature sur la Reflectivite du Silicium Oxyde: Determination Experimentale de la Sensibilite Relative; Application a la Mesure sans Contact de la Temperature a la Surface d'un Thyristor GTO en Commutation,'' Journal de Physics III, **6**, pp. 279–300.
[76] Ju, Y. S., and Goodson, K. E., 1998, ''Short-Time-Scale Thermal Mapping of Microdevices using a Scanning Thermoreflectance Technique,'' ASME J. Heat Transfer, **120**, pp. 306–313.
[77] Ju, Y. S., and Goodson, K. E., 1997, ''Thermal Mapping of Interconnects Subjected to Brief Electrical Stresses,'' IEEE Electron Device Lett., **18**, pp. 512–514.
[78] Decker, D. L., and Hodgkin, V. A., 1981, ''Wavelength and Temperature Dependence of the Absolute Reflectance of Metals at Visible and Infrared Wavelengths,'' in *National Bureau of Standards Special Publication*, NBS-SP-620, Washington, D.C.
[79] Rosei, R., and Lynch, D. W., 1972, ''Thermomodulation Spectra of Al, Au, and Cu,'' Phys. Rev. B, **5**, pp. 3883–3893.
[80] Betzig, E., and Trautman, J. K., 1992, ''Near-Field Optics: Microscopy, Spectroscopy, and Surface Modification Beyond the Diffraction Limit,'' Science, **257**, pp. 189–195.
[81] Boudreau, B. D., Raja, J., Hocken, R. J., Patterson, S. R., and Patten, J., 1997, ''Thermal Imaging With Near-Field Microscopy,'' Rev. Sci. Instrum., **68**, pp. 3096–3098.
[82] Goodson, K. E., and Asheghi, M., 1997, ''Near-Field Optical Thermometry,'' Microscale Thermophys. Eng., **1**, pp. 225–235.
[83] Bethe, H. A., 1944, ''Theory of Diffraction by Small Holes,'' The Physical Review, **66**, pp. 163–182.
[84] Mansfield, S. M., and Kino, G. S., 1990, ''Solid Immersion Microscope,'' Appl. Phys. Lett., **57**, pp. 2615–2616.
[85] Terris, B. D., Mamin, H. J., Rugar, D., Studenmund, W. R., and Kino, G. S., 1994, ''Near-Field Optical-Data Storage Using a Solid Immersion Lens,'' Appl. Phys. Lett., **65**, pp. 388–390.
[86] Ghislain, L. P., Elings, V. B., Crozier, K. B., Manalis, S. R., Minne, S. C., Wilder, K., Kino, G. S., and Quate, C. F., 1999, ''Near-Field Photolithography with a Solid Immersion Lens,'' Appl. Phys. Lett., **74**, pp. 501–503.
[87] Fletcher, D. A., Crozier, K. B., Quate, C. F., Kino, G. S., Goodson, K. E., Simanovskii, D., and Palanker, D. V., 2000, ''Near-Field Infrared Imaging with a Microfabricated Solid Immersion Lens,'' Appl. Phys. Lett., **77**, pp. 2109–2111.
[88] Fletcher, D. A., 2001, ''Near-Field Microscopy with a Microfabricated Solid Immersion Lens,'' Ph.D. thesis, Department of Mechanical Engineering, Stanford University, Stanford, CA.
[89] Goodson, K. E., and Ju, Y. S., 1999, ''Heat Conduction in Novel Electronic Films,'' *Annual Review of Materials Science*, E. N. Kaufmann et al., eds., Annual Reviews, Palo Alto, CA, Vol. 29, pp. 261–293.
[90] Cahill, D. G., 1997, ''Heat Transport in Dielectric Thin-Films and at Solid-Solid Interfaces,'' Microscale Thermophys. Eng., **1**, pp. 85–109.
[91] Chen, G., and Neagu, M., 1997, ''Thermal Conductivity and Heat Transfer in Superlattices,'' Appl. Phys. Lett., **71**, pp. 2761–2763.
[92] Hyldgaard, P., and Mahan, G. D., 1997, ''Phonon Superlattice Transport,'' Phys. Rev. B, **56**, pp. 10754–10757.
[93] Chen, G., 1998, ''Thermal-Conductivity and Ballistic-Phonon Transport in the Cross-Plane Direction of Superlattices,'' Phys. Rev. B, **57**, pp. 14958–14973.
[94] Swartz, E. T., and Pohl, R. O., 1989, ''Thermal Boundary Resistance,'' Rev. Mod. Phys., **61**, pp. 605–668.
[95] Graebner, J. E., 1993, ''Thermal Conductivity of CVD Diamond: Techniques and Results,'' Diamond Films Technol., **3**, pp. 77–130.
[96] Touzelbaev, M. N., and Goodson, K. E., 1998, ''Applications of Micron-Scale

Diamond Layers for the IC and MEMS Industries,'' Diamond Relat. Mater., **7**, pp. 1–14.
[97] Kurabayashi, K., Asheghi, M., Touzelbaev, M. N., and Goodson, K. E., 1999, ''Measurement of the Thermal Conductivity Anisotropy in Polyimide Films,'' J. Microelectromech. Syst., **8**, pp. 180–191.
[98] Bauer, S., and Dereggi, A. S., 1996, ''Pulsed Electrothermal Technique for Measuring the Thermal-Diffusivity of Dielectric Films on Conducting Substrates,'' J. Appl. Phys., **80**, pp. 6124–6128.
[99] Rogers, J. A., Yang, Y., and Nelson, K. A., 1994, ''Elastic-Modulus and In-Plane Thermal Diffusivity Measurements in Thin Polyimide Films Using Symmetry-Selective Real-Time Impulsive Stimulated Thermal Scattering,'' Appl. Phys. A: Solids Surf., **58**, pp. 523–534.
[100] Goodson, K. E., and Flik, M. I., 1994, ''Solid-Layer Thermal Conductivity Measurement Techniques,'' Appl. Mech. Rev., **47**, pp. 101–112.
[101] Cahill, D. G., 1990, ''Thermal Conductivity Measurement from 30-K to 750-K: The 3-Omega Method,'' Rev. Sci. Instrum., **61**, pp. 802–808.
[102] Cahill, D. G., and Allen, T. H., 1994, ''Thermal-Conductivity of Sputtered and Evaporated SiO_2 and TiO_2 Optical Coatings,'' Appl. Phys. Lett., **65**, pp. 309–311.
[103] Lee, S. M., and Cahill, D. G., 1997, ''Heat-Transport in Thin Dielectric Films,'' J. Appl. Phys., **81**, pp. 2590–2595.
[104] BorcaTasciuc, T., Liu, W. L., Liu, J. L., Zeng, T. F., Song, D. W., Moore, C. D., Chen, G., Wang, K. L., Goorsky, M. S., Radetic, T., Gronsky, R., Koga, T., and Dresselhaus, M. S., 2000, ''Thermal Conductivity of Symmetrically Strained Si/Ge Superlattices,'' Superlattices Microstruct., **28**, pp. 199–206.
[105] Ju, Y. S., Kurabayashi, K., and Goodson, K. E., 1999, ''Thermal Characterization of Anisotropic Thin Fielectric Films using Harmonic Joule Heating,'' Thin Solid Films, **339**, pp. 160–164.
[106] Ju, Y. S., and Goodson, K. E., 1999, ''Phonon Scattering in Silicon Films of Thickness below 100 nm,'' Appl. Phys. Lett., **74**, pp. 3005–3007.
[107] Ju, Y. S., and Goodson, K. E., 1999, ''Process-Dependent Thermal Transport Properties of Silicon Dioxide Films Deposited Using Low-Pressure Chemical Vapor Deposited,'' J. Appl. Phys., **85**, pp. 7130–7134.
[108] Goodson, K. E., Flik, M. I., Su, L. T., and Antoniadis, D. A., 1994, ''Prediction and Measurement of the Thermal Conductivity of Amorphous Dielectric Layers,'' ASME J. Heat Transfer, **116**, pp. 317–324.
[109] Tai, Y. C., Mastrangelo, C. H., and Muller, R. S., 1988, ''Thermal-Conductivity of Heavily Doped Low-Pressure Chemical Vapor-Deposited Polycrystalline Silicon Films,'' J. Appl. Phys., **63**, pp. 1442–1447.
[110] Paul, O. M., Korvink, J., and Baltes, H., 1994, ''Determination of the Thermal-Conductivity of Cmos IC Polysilicon,'' Sens. Actuators A, **41**, pp. 161–164.
[111] Kaeding, O. W., Skurk, H., and Goodson, K. E., 1993, ''Thermal Conduction in Metallized Silicon-Dioxide Layers on Silicon,'' Appl. Phys. Lett., **65**, pp. 1629–1631.
[112] Goodson, K. E., Kaeding, O. W., Roesler, M., and Zachai, M., 1995, ''Experimental Investigation of Thermal Conduction normal to Diamond-Silicon Boundaries,'' J. Appl. Phys., **77**, pp. 1385–1392.
[113] Kading, O. W., Skurk, H., Maznev, A. A., and Matthias, E., 1995, ''Transient Thermal Gratings at Surfaces for Thermal Characterization of Bulk Materials and Thin-Films,'' Appl. Phys. A: Mater. Sci. Process., **61**, pp. 253–261.
[114] Special Issue of *IEEE Transactions on Electron Devices*, 1998, Vol. 45.
[115] Davis, J. A., Venkatesan, R., Kaloyeros, A., Beylansky, M., Souri, S. J., Banerjee, K., Saraswat, K. C., Rahman, A., Reif, R., and Meindl, J. D., 2001, ''Interconnect Limits on Gigascale Integration (GSI) in the 21st Century,'' Proc. IEEE, **89**, pp. 305–324.
[116] King, W. P., Kenny, T. W., Goodson, K. E., Cross, G., Despont, M., Durig, U., Rothuizen, H., Binnig, G. K., and Vettiger, P., 2001, ''Atomic Force Microscope Cantilevers for Combined Thermomechanical Data Writing and Reading,'' Appl. Phys. Lett., **78**, pp. 1300–1302.
[117] Holland, M. G., 1963, ''Analysis of Lattice Thermal Conductivity,'' Phys. Rev., **132**, pp. 2461–2471.
[118] Asheghi, M., Touzelbaev, M. N., Goodson, K. E., Leung, Y. K., and Wong, S. S., 1998, ''Temperature-Dependent Thermal Conductivity of Single-Crystal Silicon Layers in SOI Substrates,'' ASME J. Heat Transfer, **120**, pp. 30–36.
[119] Asheghi, M., Kurabayashi, K., Goodson, K. E., Kasnavi, R., and Plummer, J. D., 1999, ''Thermal Conduction in Doped Silicon Layers,'' *Proc. 33rd ASME/AIChE National Heat Transfer Conference*, Albuquerque, NM, August 8–14.
[120] Uher, C., 1990, ''Thermal Conductivity of High-T_c Superconductors,'' J. Supercond., **3**, pp. 337–389.
[121] Richardson, R. A., Peacor, S. D., Uher, C., and Nori, F., 1992, ''$YBa_2Cu_3O_{7-\delta}$ Films: Calculation of the Thermal Conductivity and Phonon Mean Free Path,'' J. Appl. Phys., **72**, pp. 4788–4791.
[122] Goodson, K. E., and Flik, M. I., 1993, ''Electron and Phonon Thermal Conduction in Epitaxial High-T_c Superconducting Films,'' ASME J. Heat Transfer, **115**, pp. 17–25.
[123] Chen, G., 1996, ''Heat Transfer in Micro and Nanoscale Photonic Devices,'' in Tien, C.-L., editor, *Annual Review of Heat Transfer*, pp. 1–57. Begell House, New York.
[124] Mahan, G. D., and Woods, L. M., 1998, ''Multilayer Thermionic Refrigeration,'' Phys. Rev. Lett., **80**, pp. 4016–4019.
[125] Mahan, G. D., 1998, ''Good Thermoelectrics,'' in H. Ehrenreich and F. Spaepen, ed., Solid State Physics, Vol. 51, Academic Press, New York, pp. 81–157.
[126] Cahill, D. G., Bullen, A., and Lee, S.-M., 2000, ''Interface Thermal Conductance and the Thermal Conductivity of Multilayer Thin Films,'' High Temperatures High Pressures, **32**, pp. 135–142.
[127] Cahill, D. G., 1998, ''Heat Transport in Dielectric Thin Films and at Solid-Solid Interfaces,'' in C.-L. Tien, A. Majumdar, and F. M. Gerner, eds., *Microscale Energy Transport*, Taylor & Francis, Washington, DC, pp. 95–117.
[128] Young, D. A., and Maris, H. J., 1989, ''Lattice-Dynamical Calculations of the Kapitza Resistance Between FCC Lattices,'' Phys. Rev. B, **40**, pp. 3685–3693.
[129] Pettersson, S., and Mahan, G. D., 1990, ''Theory of the Thermal Boundary Resistance Between Dissimilar Lattices,'' Phys. Rev. B, **42**, pp. 7386–7390.
[130] Sergeev, A. V., 1998, ''Electronic Kapitza Conductance Due to Inelastic Electron-Boundary Scattering,'' Phys. Rev. B, **58**, pp. R10199–10202.
[131] Kechrakos, D., 1991, ''The Role of Interface Disorder in the Thermal Boundary Conductivity Between Two Crystals,'' J. Phys.: Condens. Matter, **3**, pp. 1443–1452.
[132] Streib, H. M., and Mahler, G., 1987, ''Lattice Theory of Ideal Hetero Structures: Influence of Interface Models on Phonon Propagation,'' Z. Phys. B-Condensed Matter, **65**, pp. 483–490.
[133] Kim, E.-K., Kwun, S.-I., Lee, S.-M., Seo, H., and Yoon, J.-G., 2000, ''Thermal Boundary Resistance at $Ge_2Sb_2Te_5$ /ZnS:SiO_2 Interface,'' Appl. Phys. Lett., **76**, pp. 3864–3866.
[134] Cahill, D. G., and Lee, S.-M., 1997, ''Influence of Interface Conductance on the Apparent Thermal Conductivity of Thin Films,'' Microscale Thermophys. Eng., **1**, pp. 47–52.
[135] Lee, S.-M., Matamis, G., Cahill, D. G., and Allen, W. P., 1998, ''Thin Film Materials and the Minimum Thermal Conductivity,'' Microscale Thermophys. Eng., **2**, pp. 31–36.
[136] An, K., Ravichandran, K. S., Dutton, R. E., and Semiatin, S. L., 1999, ''Microstructure, Texture, and Thermal Conductivity of Single-Layer and Multilayer Thermal Barrier Coatings of Y_2O_3-stabilized ZrO_2 and Al_2O_3 Made by Physical Vapor Deposition,'' J. Am. Ceram. Soc., **82**, pp. 399–406.
[137] Soyez, G., Eastman, J. A., Thompson, L. J., Bai, G.-R., Baldo, P. M., McCormick, A. W., DiMelfi, R. J., Elmustafa, A. A., Tambwe, M. F., and Stone, D. S., 2000, ''Grain-Size-Dependent Thermal Conductivity of Nanocrystalline Yttria-Stabilized Zirconia Films Grown by Metal-Organic Chemical Vapor Deposition,'' Appl. Phys. Lett., **77**, pp. 1155–1157.
[138] Hyldegaard, P., and Mahan, G. D., 1997, ''Phonon Superlattice Transport,'' Phys. Rev. B, **56**, pp. 10754–10757.
[139] Ichiro Tamura, S., Tanaka, Y., and Maris, H. J., 1999, ''Phonon Group Velocity and Thermal Conduction in Superlattices,'' Phys. Rev. B, **60**, pp. 2627–2630.
[140] Kiselev, A. A., Kim, K. W., and Stroscio, M. A., 2000, ''Thermal Conductivity of Si/Ge Superlattices:A Realistic Model With a Diatomic Unit Cell,'' Phys. Rev. B, **62**, pp. 6896–6899.
[141] Bies, W. E., Radtke, R. J., and Ehrenreich, H., 2000, ''Phonon Dispersion Effects and the Thermal Conductivity Reduction in GaAs/AlAs Superlattices,'' J. Appl. Phys., **88**, pp. 1498–1503.
[142] Lee, S.-M., Cahill, D. G., and Venkatasubramanian, R., 1997, ''Thermal Conductivity of Si-Ge Superlattices,'' Appl. Phys. Lett., **70**, pp. 2957–2959.
[143] Simkin, M. V., and Mahan, G. D., 2000, ''Minimum Thermal Conductivity of Superlattices,'' Phys. Rev. Lett., **84**, pp. 927–930.
[144] Afromowitz, M. A., 1973, ''Thermal Conductivity of GaAlAs Alloys,'' J. Appl. Phys., **44**, pp. 1292–1294.
[145] Liu, W. L., Borca-Tasciuc, T., Chen, G., Liu, J. L., and Wang, K. L., 2001, ''Anisotropic Thermal Conductivity of Ge Quantum-Dot and Symmetrically Strained Si/Ge Superlattices,'' J. Nanosci. Nanotech., **1**, pp. 39–42.
[146] VonArx, M., Paul, O., and Baltes, H., 2000, ''Process-Dependent thin-Film Thermal Conductivities for Thermal CMOS MEMS,'' J. Microelectromech. Syst., **9**, pp. 136–145.
[147] Uma, S., McConnell, A. D., Asheghi, M., Kurabayashi, K., and Goodson, K. E., 2000, ''Temperature Dependent Thermal Conductivity of Undoped Polycrystalline Silicon Layers,'' Int. J. Thermophys., in press.
[148] McConnell, A. D., Srinivasan, U., Asheghi, M., and Goodson, K. E., 2002, ''Thermal Conductivity of Doped Polysilicon,'' J. Microelectromech. Syst., in press.
[149] Ziman, J. M., 1960, *Electrons and Phonons*, Oxford University Press, Oxford, United Kingdom.
[150] Verhoeven, H., Boettger, E., Floter, A., Reiss, H., and Zachai, R., 1997, ''Thermal-Resistance and Electrical Insulation of Thin Low-Temperature-Deposited Diamond Films,'' Diamond Relat. Mater., **6**, pp. 298–302.
[151] Goodson, K. E., 1996, ''Thermal Conduction in Nonhomogeneous CVD Diamond Layers in Electronic Microstructures,'' ASME J. Heat Transfer, **118**, pp. 279–286.
[152] Goodson, K. E., Flik, M. I., Su, L. T., and Antoniadis, D. A., 1993, ''Annealing-Temperature Dependence of the Thermal Conductivity of LPCVD Silicon-Dioxide Layers,'' IEEE Electron Device Lett., **14**, pp. 490–492.
[153] Cahill, D. G., Watson, S. K., and Pohl, R. O., 1992, ''Lower Limit to the Thermal Conductivity of Disordered Crystals,'' Phys. Rev. B, **46**, pp. 6131–6140.
[154] Alivisatos, A. P., 1996, ''Semiconductor Clusters, Nanocrystals, and Quantum Dots,'' Science, **271**, pp. 933–936.
[155] Duan, X., and Lieber, C. M., 2000, ''General Synthesis of Compound Semiconductor Nanowires,'' Adv. Mater., **12**, pp. 298–302.
[156] Morales, A. M., and Lieber, C. M., 1998, ''A Laser Ablation Method for the Synthesis of Crystalline Semiconductor Nanowires,'' Science, **279**, pp. 208–211.
[157] Yiying, W., and Yang, P., 2000, ''Germanium/Carbon Core-Sheath Nanostructures,'' Appl. Phys. Lett., **77**, pp. 43–45.
[158] Cui, Y., Lauhon, L. J., Gudiksen, M. S., Wang, J. F., and Lieber, C. M., 2001, ''Diameter-Controlled Synthesis of Single-Crystal Silicon Nanowires,'' Appl. Phys. Lett., **78**, pp. 2214–2216.
[159] Cui, Y., and Lieber, C. M., 2001, ''Functional Nanoscale Electronic Devices

Assembled Using Silicon Nanowire Building Blocks,'' Science, **291**, pp. 851–853.
[160] Lin, Y. M., Cronin, S. B., Ying, J. Y., Dresselhaus, M. S., and Heremans, J. P., 2000, ''Transport Properties of Bi Nanowire Arrays,'' Appl. Phys. Lett., **76**, pp. 3944–3946.
[161] Chung, S. W., Yu, J. W., and Heath, J. R., 2000, ''Silicon Nanowire Devices,'' Appl. Phys. Lett., **76**, pp. 2068–2070.
[162] Zhang, Z. B., Sun, X. Z., Dresselhaus, M. S., Ying, J. Y., and Heremans, J., 2000, ''Electronic Transport Properties of Single-Crystal Bismuth Nanowire Arrays,'' Phys. Rev. B, **61**, pp. 4850–4861.
[163] Schwab, K., Henriksen, E. A., Worlock, J. M., and Roukes, M. L., 2000, ''Measurement of Quantum Conductance of Thermal Conductance,'' Nature (London), **404**, pp. 974–977.
[164] Santamore, D. H., and Cross, M. C., 2001, ''Effect of Phonon Scattering by Surface Roughness on Universal Thermal Conductance,'' Phys. Rev. Lett., **87**, pp. 115502.
[165] Volz, S., and Lemonnier, D., 2000, ''Confined Phonon and Size Effects on Nanowire Thermal Conductivity. The Radiative Transfer Approach,'' Phys. Low-Dimensional Structures, **5–6**, pp. 91–107.
[166] Zou, J., and Balandin, A., 2001, ''Phonon Heat Conduction in a Semiconductor Nanowire,'' J. Appl. Phys., **89**, pp. 2932–2938.
[167] Hone, J., Whitney, M., Piskoti, C., and Zettl, A., 1999, ''Thermal Conductivity of Single-Walled Carbon Nanotubes,'' Phys. Rev. B, **59**, pp. R2514–R2516.
[168] Berber, S., Kwon, Y.-K., and Tomanek, D., 2000, ''Unusually High Thermal Conductivity of Carbon Nanotubes,'' Phys. Rev. Lett., **84**, pp. 4613–4616.
[169] Kim, P., Shi, L., Majumdar, A., and McEuen, P., 2001, ''Thermal Transport Measurements of Individual Multiwall Carbon Nanotubes,'' Phys. Rev. Lett., **87**, pp. 215502 (1–4).
[170] Borca-Tasciuc, T., Achimov, D., Liu, W. L., Chen, G., Ren, H.-W., Lin, C.-H., and Pei, S. S., 2001, ''Thermal Conductivity of InAs/AlSb superlattices,'' Microscale Thermophys. Eng., **6**, in press.